UNIVERSIDADE FEDERAL DE MINAS GERAIS

Instituto de Geociências

Programa de Pós-Graduação em Geologia

Ramon de Oliveira Aranda

PETROLOGY OF THE AFONSO CLÁUDIO INTRUSIVE COMPLEX (ESPÍRITO SANTO STATE, ARAÇUAÍ OROGEN): insights from petrography, lithogeochemistry, U-Pb geochronology and Lu-Hf isotopes

Nº 188

Belo Horizonte

03/08/2018

Ramon de Oliveira Aranda

PETROLOGY OF THE AFONSO CLÁUDIO INTRUSIVE COMPLEX (ESPÍRITO SANTO STATE, ARAÇUAÍ OROGEN): insights from petrography, lithogeochemistry, U-Pb geochronology and Lu-Hf isotopes

Versão Final

Dissertação apresentada ao programa de Pós-Graduação em Geologia do Instituto de Geociências da Universidade Federal de Minas Gerais como requisito para obtenção do título de mestre em Geologia.

Área de Concentração: Geologia Regional

Orientador: Prof. Dr. Alexandre de Oliveira Chaves

Coorientador: Prof. Dr. Edgar Batista de Medeiros Júnior

Belo Horizonte

2018

A662p Aranda, Ramon de Oliveira.

2018 Petrology of The Afonso Cláudio Intrusive Complex (Espírito Santo State, Araçuaí Orogen) [manuscrito]: insights from petrography, lithogeochemistry, U-Pb geochronology and Lu-Hf isotopes / Ramon de Oliveira Aranda – 2018.
57f., enc. (principalmente color.)

Orientador: Alexandre de Oliveira Chaves.

Coorientador: Edgar Batista de Medeiros Júnior.

Dissertação (mestrado) – Universidade Federal de Minas Gerais, Instituto de Geociências, 2018.

Área de concentração: Geologia Regional.

Bibliografia: f. 40-47.

Inclui anexos.

1. Petrologia – Espírito Santo – Teses. 2. Geoquímica – Espírito Santo – Teses. 3. Tempo geológico – Teses. 4. Isótopos – Teses. I. Chaves, Alexandre de Oliveira. II. Medeiros Júnior, Edgar Batista de. III. Universidade Federal de Minas Gerais. Instituto de Geociências. IV. Título.

CDU: 552 (815.2)

Ficha catalográfica elaborada por Graciane A. de Paula – CRB6 3404

UNIVERSIDADE FEDERAL DE MINAS GERAIS

PROGRAMA DE PÓS-GRADUAÇÃO EM GEOLOGIA

FOLHA DE APROVAÇÃO

Petrology of the Afonso Cláudio Intrusive Complex (Araçuaí Orogen): insights from petrography, lithogeochemistry, U-Pb geochronology, and Lu-Hf isotopes

RAMON DE OLIVEIRA ARANDA

Dissertação submetida à Banca Examinadora designada pelo Colegiado do Programa de Pós-Graduação em GEOLOGIA, como requisito para obtenção do grau de Mestre em GEOLOGIA, área de concentração GEOLOGIA REGIONAL.

Aprovada em 03 de agosto de 2018, pela banca constituída pelos membros:

Prof. Alexandre de Oliveira Chaves - Orientador
UFMG

Prof. Adolf Heinrich Horn
UFMG

Prof. Rodson de Abreu Marques
UFES

Belo Horizonte, 3 de agosto de 2018.

Ao meu amado tio, que descansa aos braços do senhor!

To my dear uncle, who rests in the God arms!

AGRADECIMENTOS

Sou grato em primeiro lugar a Deus! Pelo dom da vida, por minha família e por toda a força que ELE me envia nos momentos de dificuldade.

À minha família, que apesar da distância se faz presente, com o apoio incondicional, amor, incentivo e por toda torcida. À minha mãe, Serenuza Almeida de Oliveira, obrigado pelo incentivo, por todo amor e confiança depositados em mim. À minha vó, Elza Almeida de Oliveira, obrigado pelas orações, pelo amor e por entender meus momentos de ausência. À minha tia, Rosângela Almeida de Oliveira, por todo amor, carinho e esforço. À meu PAIdrasto, Helder José dos Santos, pela amizade e confiança. Agradeço ao meu tio, José Carlos Almeida Oliveira, pelo companheirismo e por me mostrar que o verdadeiro amor existe apesar de todas as diferenças! Obrigado!

À Rex e Renna por todos os momentos compartilhados e por me mostrarem que o verdadeiro amor se encontra em pequenos gestos!

À minha namorada, Letícia Gomes de Carvalho, pelo apoio nos momentos difíceis, amizade, companheirismo, incentivo e compreensão dos meus momentos de ausência. À toda a sua família pelo acolhimento, incentivo e amizade!

Ao meu orientador, Alexandre de Oliveira Chaves, por toda a ajuda, paciência, boa vontade, transferência de conhecimento e pela amizade construída ao longo destes dois anos de trabalho!

Também agradeço ao meu coorientador, Edgar Batista de Medeiros Júnior, pela imensa ajuda, desde quando este trabalho era apenas uma ideia até a conclusão desta dissertação e pela amizade construída ao longo destes anos!

À todos que de alguma forma colaboraram para a construção desse trabalho! André Corado, Daniel Peterle, Afonso Bozzi, Ledson Sathler, Iuri Lobão, obrigado pela ajuda nas atividades de campo. Ao Vinícius Carnielli e sua família pela hospedagem e boa vontade de ajudar! Agradeço especialmente ao meu amigo Ricardo Venturini, pela imensa ajuda desde o princípio deste trabalho! Sem vocês este trabalho ainda seria apenas uma ideia!

À todos os amigos da pós, em especial Arnon, Rodrigo, Leandro, Pedro Leonardo, Diego e Matheus. Pelas experiências compartilhadas, momentos compartilhados, discussões geológicas e por toda amizade construída!

Aos amigos/funcionários do CPMTC, Carlos, Jhonny, Leo, Hélvio e Denise pela amizade e boas risadas compartilhas.

Ao Conselho Nacional de Desenvolvimento Científico e Tecnológico (CNPq) pela bolsa de estudos.

À Pró-reitoria de Pós-graduação (PRPg) da UFMG, ao Programa de Pós-graduação em Geologia do Instituto de Geociências (IGC) da UFMG e ao CPMTC pelo apoio estrutural;

Aos meus colegas de república Marcelo e Danilo.

À todos meus amigos e à todas pessoas que de alguma forma contribuíram para a realização deste trabalho!

O presente trabalho foi realizado com apoio da Coordenação de Aperfeiçoamento de Pessoal de Nível Superior - Brasil (Capes) - Código de Financiamento 001.

Enfim, muito obrigado a todos!

Eu nunca perco. Ou eu ganho, ou aprendo (Nelson Mandela).

I never lose. I either win or learn (Nelson Mandela).

RESUMO

O Complexo Intrusivo Afonso Cláudio (ACIC, em inglês) é um corpo ígneo de forma quase elíptica com aproximadamente 73 km² de área. É localizado no estado do Espírito Santo, no sudeste do Brasil, e se insere com contexto geológico dos granitoides pós-colisionais (Supersuíte G5) do sistema orogênico Araçuaí-Congo Ocidental (AWCO, em inglês). Estes granitoides são associados a fase de colapso extensional (530-490 Ma) deste sistema orogênico e tem evolução associada a interação entre magmas mantélicos e crustais. Neste trabalho foram integrados dados de mapeamento geológico, petrografia, litoquímica, geocronologia U-Pb e isótopos de Lu-Hf com intuito de entender os processos ígneos que atuaram neste corpo ígneo. O ACIC está encaixado em ortognaisses da Supersuíte G1 do AWCO (granitoides pré-collisionais de idade entre 630-580 Ma) e paragnaisses neoproterozóicos do Complexo Nova Venécia. É constituído por dois núcleos máficos compostos de monzogabro e monzodiorito, circundados por quartzo monzonito. Entre estas rochas ocorrem zonas de mistura de magmas física (*mingling*) e química (*mixing*), onde jotunito e quartzo mangerito ocorrem localmente. Xenólitos de rochas encaixantes são encontrados no monzogabro, monzodiorito e no quartzo monzonito, assim como enclaves de monzogabro e monzodiorito, quase sempre circulares, são encontrados no quartzo monzonito. Ambas as rochas, máficas e félsicas, são enriquecidas em LILE e LREE, além disso, ambas mostram assinatura geoquímica álcali-cálcica de ambiente tectônico pós-colisional. Datação U-Pb em zircão revelou idades de cristalização magmática de 480,9 ±- 3,2 Ma para quartzo monzonito e 496,5 ± 3,6 Ma para monzogabro. Ambos litotipos possuem valores negativos de εHf em zircão (os valores médios são -11,78 para o quatzo monzonito e -10,41 para o monzogabro) e idades T_{DM} de 1,79 Ga para o quartzo monzonito e 1,72 Ga para o monzogabro. Nossos resultados indicam que algum processo de contaminação crustal ocorreu nos magmas do ACIC antes ou durante a intrusão deste corpo ígneo. Falhas profundas relacionadas a forças extensionais, geradas no colapso orogênico, e a descompressão associada podem explicar os processos de fusão em crosta inferior e no manto litosférico e a subsequente ascensão dos magmas. São propostos dois modelos para a evolução do ACIC durante o estágio de colapso do AWCO. Ambos os modelos envolvem processos de contaminação crustal e assimilação somados a cristalização fracionada (processos AFC). Um dos modelos é a favor de contemporânea fusão crustal e mantélica, onde os magmas gerados teriam interagido para gerar um magma mais rico em álcalis. A cristalização deste magma teria produzido o monzogabro e o monzodiorito. Com a continuidade do colapso do orógeno, estas

rochas máficas álcali-cálcicas recém formadas teriam se fundido parcialmente e gerado um magma monzonítico, do qual cristalizou o quartzo monzonito. Os enclaves máficos neste modelo seriam considerados como resíduos da fusão do monzogabbro e monzodiorito. O segundo modelo argumenta em favor de uma intrusão de um magma máfico mantélico em uma câmara magmática já preenchida com um magma félsico crustal. Estes magmas teriam interagido entre si e o magma máfico teria formado o monzogabro e o monzodiorito através de sua cristalização, enquanto o magma félsico teria formado o quartzo monzonito. Neste modelo, os enclaves máficos são interpretados como injeções do magma máfico no magma félsico. Ambos modelos podem ser sustentados pelas idades T_{DM} e pelos valores εHf dos zircões. Nos dois modelos as zonas de mistura química e física de magmas seriam geradas pela interação dos magmas félsicos e máficos. Evidências de cisalhamento são encontradas localmente onde aflora o quartzo monzonito (principalmente nas bordas do ACIC) e estas evidencias podem indicar que alguma força transtensional atuou na região até o fim do resfriamento das rochas do ACIC. Devido à similaridade entre os plutons da Supersuíte G5 do AWCO, os modelos propostos para o ACIC também poderiam explicar a petrogênese de alguns outros plutons desta supersuíte.

Palavras-chave: Complexo Intrusivo Afonso Cláudio; petrogênese; geoquímica; geocronologia U-Pb, isótopos de Lu-Hf; Orógeno Araçuaí-Congo Ocidental.

ABSTRACT

The Afonso Cláudio Intrusive Complex (ACIC) is a ca. 73 km² igneous body located in the Espírito Santo state, Southeastern Brazil. It is inserted in the geologic context of the post-collisional G5 plutonic Supersuite related to the extensional collapse stage (530-490 Ma) of the Araçuaí-West Congo Orogen (AWCO). The G5 plutons evolution is related to interaction between mantle and crustal magmas. In this study we have integrated field relationships, petrography, lithogeochemistry, U-Pb geochronology, and Lu-Hf isotopes to understand the ACIC petrology. The ACIC is hosted in pre-collisional orthogneisses of the AWCO G1 Supersuite (630-580 Ma) and Neoproterozoic paragneisses of the Nova Venécia Complex. This plutonic body is constituted by two monzogabbro/monzodiorite mafic cores surrounded by quartz monzonite. There are mingling and mixing zones between these rocks, where jotunite and quartz mangerite occur. In addition, there are host rock enclaves in the monzograbbro, monzodiorite and quartz monzonite, as well as rounded monzogabbro/monzodiorite enclaves in the quartz monzonite. The mafic and felsic rocks are enriched in LILE and LREE and they have alkali-calcic post-collisional geochemical signature. Zircon U-Pb dating revealed crystallization ages of 480.9 ± 3.2 Ma to quartz monzonite and 496.5 ± 3.6 Ma to monzogabbro. Both quartz monzonite and monzogabbro show negative zircon εHf values (the average values are -11.78 to quartz monzonite and -10.41 to monzogabbro) and average T_{DM} age of 1.79 Ga to quartz monzonite and 1.72 Ga to monzogabbro. These results indicate that crustal contamination process occurred before or during the emplacement of this igneous body. Deep faulting related to the extensional forces during the orogenic collapse and the associated decompression can explain lower crust and mantle melting and subsequent magma rising. Based on presented data, two models are proposed to the ACIC evolution during the collapse stage of the AWCO. Both models involve crustal contamination and assimilation more fractional crystallization (AFC). One is based on coeval mantle and crustal melting, with magmas interaction to generate an alkali-calcic magma, whose crystallization produced the monzogabbro and monzodiorite. With collapse continuity, these mafic rocks would have melted and generated felsic magmas that crystalized as quartz monzonite. This model is supported by zircon εHf and T_{DM} data and it considers mafic enclaves as residuals of monzogabbro/monzodiorite. Our second model argues that mantle magma intruded in a magmatic chamber loaded by crustal felsic magma, with subsequent interaction between them. Monzogabbro and monzodiorite would have been generated by fractional crystallization of the

mafic magmas, while the quartz monzonite by the crystallization of the felsic magmas. The mafic enclaves could be interpreted as mafic magma blobs inside felsic magma in this model. The zircon εHf and T_{DM} data also support this one. In both models, the mingling and mixing zones were generated by the interaction between the mafic and felsic magmas. Shear evidences were mapped in the quartz monzonite at ACIC edge and could be an evidence that there was any transtensional force acting until the ACIC cooled. Due to the similarities among the post-collisional plutons in the AWCO, these models can be used to explain the petrogenesis of other similar plutons of this orogenic system.

Keywords: Afonso Cláudio Intrusive Complex; petrogenesis; geochemistry; U-Pb geochronology; Lu-Hf isotopes; Araçuaí-West Congo Orogen.

LIST OF FIGURES

apatite, 1% opaque minerals and 1% zircon. The relative ratios of assimilated material to crystallized material considered was between 0.6% and 0.8%. The assimilated material considered was the lower continental crust (Taylor and McLennan, 1995). 52

LIST OF TABLES

SUMMARY

1. INTRODUCTION

The Afonso Cláudio Intrusive Complex (ACIC) is an igneous pluton located in the homonymous city, in the Espírito Santo State, Southeast Brazil. It is inserted in the geological context of the Araçuaí-West Congo Orogen (AWCO) crystalline core, where mainly occurs high-grade metamorphic rocks and a huge amount of granitic rocks, which are grouped in different geotectonic supersuites (Pedrosa-Soares and Wiedemann-Leonardos, 2000; Pedrosa-Soares et al., 2001, 2011; Alkmim et al., 2006). The ACIC is part of the post-collisional granitoids or G5 Supersuíte from AWCO (Pedrosa-Soares and Wiedemann-Leonardos, 2000; Vieira, 2015).

The ACIC has never been studied in detail and the only investigations that approached this pluton were the regional geological mappings in the Espírito Santo state in 1970', 1980', and 1990' decades (Silva and Ferrari, 1976; Paradella et al., 1978; Filho et al., 1983; Signorelli et al., 1993; Féboli et al., 1993; Vieira et al., 1993; Vieira, 2015). These studies approached remote sensing, geological mapping, petrography, and scarce lithogeochemistry of the ACIC.

This work is the first detailed work about the ACIC and it aims to contribute to better understanding of the petrology of this pluton. In addition, the present work is one of the first investigations that approach the Lu-Hf isotopes of the G5 Supersuite from Araçuaí-West Congo Orogen.

1.1. Objectives

In order to investigate the petrology of the ACIC, this work has as main objectives:

- to present the geological mapping (and field relationships), petrography, lithogeochemistry, U-Pb geochronology, and Lu-Hf isotopes of the ACIC rocks;

- to understand the igneous processes that acted in ACIC;

- to propose petrogenetic models to ACIC, which could be used to explain other similar post-collisional plutons in AWCO;

- to contribute to the geology of the Espírito Santo state;

1.2. Localization

The ACIC is located in the Afonso Cláudio town, about 140 km to Vitória, States's capital, in the named mountain region of the Espírito Santo state. The pluton is situated among the town's center and the São Francisco Xavier do Guandu and Serra Pelada districts.

There are many ways to get to the Afonso Claúdio city leaving from Vitória city. The main access is traveling by BR-101, BR-262 and ES-165 highways, accessing the last highway few kilometers before the Venda Nova do Imigrante city (Figure 1.1).

From Afonso Cláudio town center to ACIC, the access is facilitated by highways around of the ACIC (ES-165, ES-484 and ES-460) and side roads that cross part of this pluton (Figure 1.1).

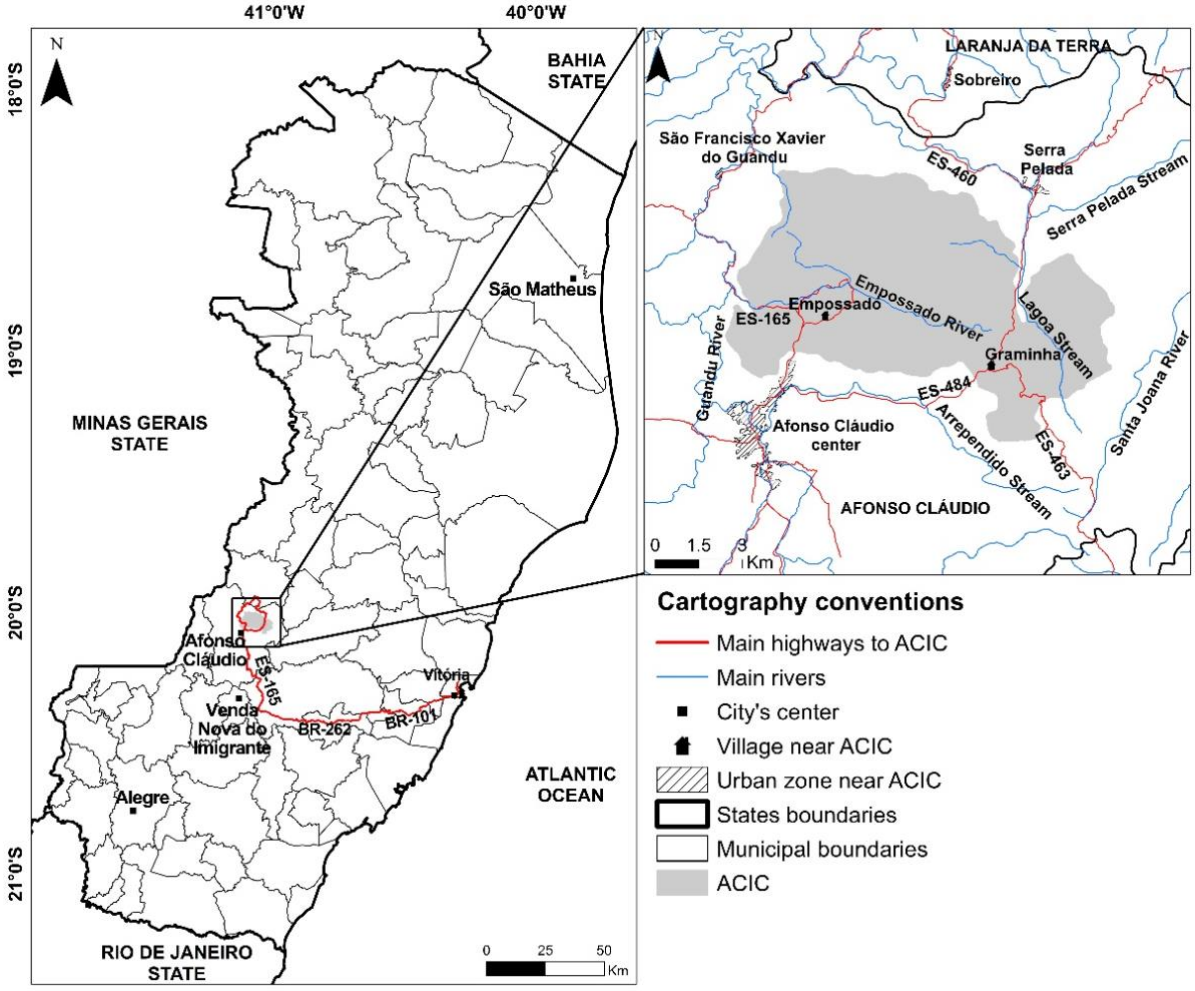

Figure 1.1: Highways to get Afonso Cláudio town from Vitória and roads to ACIC from Afonso Cláudio town.

1.3. Materials and methods

The work methodology followed the following steps:

- Bibliography review about ACIC and AWCO;
- Pre-fieldwork analyses (satellite images plus airborne geophysics maps);
- Fieldwork (geological mapping and sample collect);
- Petrography analyses (61 thin sections);
- Lithogeochemical analyses (20 samples);
- U-Pb geochronology and Lu-Hf isotopes (zircons from two samples);

The detailed methodology is described in next section (paper).

1.4. Dissertation structure

This dissertation is segmented in three chapters:

- Introduction: it aims to show the basic information about the ACIC area, as well as objectives and methodology of this work;
- Paper: it shows the main results of this work in paper format. The paper was named "Petrology of the Afonso Cláudio Intrusive Complex: New insights for the Cambro-Ordovician post-collisional magmatism in the Araçuaí-West Congo Orogen, Southeast Brazil";
- Final remarks: it presents a summary of the main ideas of this dissertation;

2. PETROLOGY OF THE AFONSO CLÁUDIO INTRUSIVE COMPLEX (SOUTHEAST BRAZIL): IMPLICATIONS FOR THE POST-COLLISIONAL MAGMATISM IN ARAÇUAÍ-WEST CONGO OROGEN

2.1. Introduction

Post-collisional calc-alkaline magmatic plutons have been studied worldwide and most of them are composed of, at least, two main rock groups, the felsic and mafic rocks (it is important to highlight that the term mafic in this paper is also referred to mesocratic igneous rocks). Some significant questions raised about these ones are "what is the petrogenetic relationship between these rock groups?" and "what are the petrologic processes that operated in the most calc-alkaline plutons worldwide?". Many researchers have argued in favor of the evolution related to fractional crystallization of one magma (Ratajeski et al., 2001; Zhang and Zhao, 2017, and references therein), while many others have emphasized an interaction between magmas from different sources, involving mingling, mixing and fractional crystallization processes (Fourcade and Allegre, 1981; Janousek et al., 2000; Ratajeski et al., 2001; De Campos et al., 2004, 2016; Liu et al., 2013; Quek et al., 2017; Sami et al., 2018).

These studies have been mainly supported by geological mapping, petrography, whole-rock lithogeochemistry, mineral chemistry, U-Pb geochronology and isotopic geology (mainly Sm-Nd and Rb-Sr systems). Some recent studies have approached the Lu-Hf isotopic system, which proves itself a suitable tool to petrogenetic investigation in magmatic and metamorphic rocks. The integrated study between U-Pb geochronology and Lu-Hf isotopes has also been recently applied to unravel the magmatic processes and magma sources of magmatic plutons worldwide (Chen et al., 2016, 2017; Zhu et al., 2018; Fourny et al., 2019; Lu et al., 2019). Zircon has been widely used in these studies, this mineral carries elevate quantities of the U and Hf, which allow U-Pb geochronology and Hf isotopes combined studies in zircon crystals (Kinny and Maas, 2003; Matteini et al., 2010; Vervoort, 2015).

The Araçuaí-West Congo Orogen (AWCO) has its evolution related to Neoproterozoic-Cambro-Ordovician Brasiliano/Pan-African orogeny, during West Gondwana amalgamation (Figure 2.1a and 2.1b). An extensive magmatism (630-480 Ma) is a relevant feature of this orogeny, which presents different stages based on geotectonic and petrologic evidences (Pedrosa-Soares and Wiedemann-Leonardos, 2000; Alkmim et al., 2006; Pedrosa-Soares et al., 2008). The Afonso Cláudio Intrusive Complex (ACIC) is part of the G5 plutonic Supersuite,

which represents the magmatism in the post-collisional stage of the AWCO (530-480 Ma) (Wiedemann et al., 2002; Valeriano et al., 2011; Vieira, 2015; De Campos et al., 2016).

The G5 plutons show calc-alkaline composition, widespread evidences of mingling and mixing processes and they are mainly constituted by three different rock groups: mafic, felsic and charnockitic rocks (Wiedemann et al., 2002; De Campos et al., 2004, 2016). As well as worldwide, the same questions about AWCO post-collisional plutons are raised. Many researchers have argued in favor to different magmatic sources among these rocks. The mafic rocks were associated to mantle magma intrusions, while the felsic rocks were related to crustal melting. The charnockitic rocks were associated to an earlier lower crust melting event during initial phase of AWCO collapse stage (Bayer et al., 1987; Ludka and Wiedemann-Leonardos, 2000; Medeiros et al., 2001; Wiedemann et al., 2002; De Campos et al., 2004, 2016; Mendes et al., 2005; Mendes and De Campos, 2012).

The ACIC is located near Afonso Cláudio town, about 152 kilometers from Vitória, the capital city of the Espírito Sante State, southeast Brazil (Figure 2.1c). Despite regional studies, this pluton has never been studied in detail. The present paper is the first geological research to be focused on the ACIC and present geological mapping data in 1:25.000 scale, petrographic features, whole-rock lithogeochemistry, zircon U-Pb geochronology and zircon Hf isotopes of the ACIC rocks. Furthermore, this paper is one of the first to approach Hf isotopes of the G5 Supersuite from AWCO and it has as main objectives to discuss about magmatic sources of the rocks and set up petrogenetic models to the ACIC, which can explain other similar G5 plutons of the AWCO.

2.2. Geological setting and the magmatism of the Araçuaí-West Congo Orogen

The study area is inserted in the Araçuaí Orogen, in Southeast Brazil, which together its African counterpart (West Congo Belt), compose the Araçuaí-West Congo Orogen (AWCO) (Figure 2.1a and 2.1b), a confined orogenic system that was formed during Brasiliano/Pan-African orogeny, between the São Francisco and Congo Cratons (Pedrosa-Soares et al., 2008, 2011). The tectonic model proposed for this orogenic system is similar to a “nutcracker” closure but catalyzed by remote collisions (Alkmim et al., 2006). The São Francisco and Congo Cratons were connected by Bahia-Gabon cratonic bridge since the Tonian and the collisions between their neighbor cratons (Paranapanema and Kalahari Cratons) caused the initial tectonic stresses

to the closure of the Adamastor Ocean, the ocean between the São Francisco and Congo Cratons, resulting the assembly of the West Gondwana and edification of the AWCO (Brito Neves and Cordani, 1991; Trompette et al., 1994; Pedrosa-Soares et al., 2001, 2008, 2011; Alkmim et al., 2006).

The AWCO shows some peculiar features, such as the remarkable granite generation and a confined nature during its evolution. The model proposed for its evolution is segmented in different stages and each stage has its own granitogenesis (Figure 2.1c) (Pedrosa-Soares and Wiedemann-Leonardos, 2000; Alkmim et al., 2006). According to these authors, the granitic rocks can be grouped in five supersuites based on its field, structural, petrography, geochemical, geochronological and isotopic features. The pre-collisional stage (630-580 Ma) produced the G1 Supersuite (related to the Rio Doce magmatic arc). The metasedimentary rocks from back-arc zone (Nova Venécia Complex) are also associated with this stage. The collisional stage (580-560 Ma) generated the G2 Supersuite and during the late collisional stage (560-530 Ma) the G3 Supersuite was formed. The post-collisional stage (530-490 Ma) produced the G4 and G5 Supersuites (Pedrosa-Soares and Wiedemann-Leonardos, 2000; Pedrosa-Soares et al., 2001, 2008, 2011; Wiedemann et al., 2002; De Campos et al., 2004, 2016; Alkmim et al., 2006; Valeriano et al., 2011; Gradim et al., 2014; Richter et al., 2016; Tedeschi et al., 2016).

The ACIC is part of the G5 Supersuite (Vieira, 2015). This one is associated to the extensional collapse of the AWCO and it is constituted by igneous bodies with about 50 up to 200 km², represented by post-collisional I and A2 type granitoids. The main characteristics of the G5 Supersuite are a general inverse concentric zoning (mafic cores surrounded by felsic rocks), mingling and mixing evidences and igneous border foliation concordant with enclosing rocks foliation. All plutons of G5 Supersuite intruded along regional weakness zones, as vertical shear zones and fold axes. The main lithotypes of the G5 supersuite range from mafic rocks as gabbro (sometimes olivine-gabbro), norite, diorite, monzogabbro, and monzodiorite to felsic rocks as monzonite, syenite, granites, tonalite and granodiorite. Some G5 plutons present outer rings of charnockitic rocks. The G5 plutons are grouped in three geochemical groups: tholeiitic, high-K calc-alkaline (90% of all plutons) and alkaline to peralkaline (Horn and Weber-Diefenbach, 1987; Pedrosa-Soares and Wiedemann-Leonardos, 2000; Medeiros et al., 2001; Pedrosa-Soares et al., 2001, 2011; Wiedemann et al., 2002; De Campos et al., 2004, 2016; Mendes et al., 2005; Mendes and De Campos, 2012). A short review of some G5 Plutons is presented in Table 2.1.

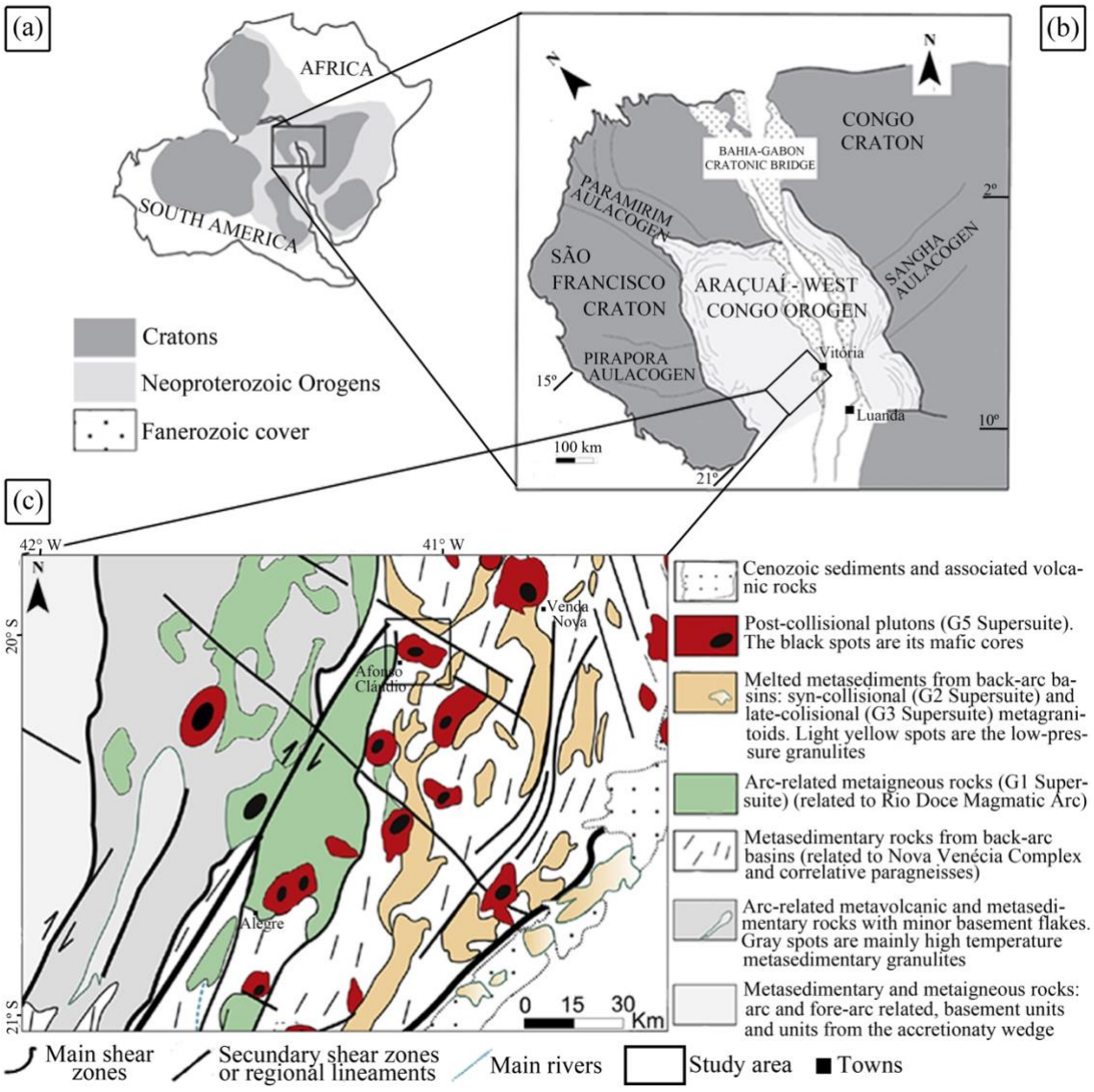

Figure 2.1: (a) and (b): Gondwana Scenario during AWCO amalgamation. Modified from: Alkmim et al. (2006); Pedrosa-Soares et al. (2001). (c): Simplified geological map of the Araçuaí Orogen's southern part, showing the regional context of the ACIC. Modified from: Bayer et al. (1987); Pedrosa-Soares et al. (2001); Wiedemann et al. (2002); De Campos et al. (2004, 2016).

Table 2.1: Summary about some post-collisional plutons from AWCO (Bayer et al., 1987; Horn & Weber-Diefenbach, 1987; Ludka et al., 1998; Ludka & Wiedemann-leonardos, 2000; Pedrosa-Soares & Wiedemann-Leonardos, 2000; Medeiros et al., 2001; Wiedemann et al., 2002; De Campos et al., 2004, 2016; Mendes et al., 2005; Mendes & De Campos, 2012; Zanon et al., 2015).

Post-collisional igneous complex	**C.a. area (km^2)**	**Main lithotypes**	**Main host rocks**	**Zircon U-Pb ages**	**εNd(t) values**	**εSr(t) values**
Santa Angélica	200	Gabbro-norite, gabbro diorite, quartz monzonite, syenogranite	Granulitic orthogneiss (G1 Supersuite), garnet-cordierite gneiss (Nova Venécia Complex)	513±8 (quartz monzonite); 492±15 (syenogranite)	-13.42 ~ -12,73 (quartz monzonite), -13.55 ~ -13.07 (gabbro/diorite)	184.28 (quartz monzonite), 43.73 ~ 47.52 (gabbro/diorite);
Castelo	100	Diorite, granodiorite, monzogranite	Granulitic orthogneiss (G1 Supersuite), garnet-cordierite gneiss and marble (Nova Venécia Complex)	Unknown	Unknown	Unknown
Varzea Alegre	150	Norite, diorite, monzodiorite, granodiorite, granite, charnockite	Granulitic orthogneiss (G1 Supersuite), garnet-cordierite gneiss (Nova Venécia Complex)	498+-5 (charnockite); 507+-3 (granite)	-7.90 (diorite); -5.34 (norite); -7.93 (granite); -10.10 ~ -8.38 (chanockite)	47.62 (diorite); -48.10 (norite); -64.84 (granite); -65.49 ~ 109.72 (chanockite)
Pedra Azul/Aracê	200	Diorite, Granodiorite, tonalite and granite	Granulitic orthogneiss (G1 Supersuite), garnet-cordierite gneiss and sillimanitequartzite (Nova Venécia Complex)	Unknown	Unknown	Unknown
Venda Nova	75	Gabbro, norite, syeno-monzonite, monzodiorite,	Ortho- and paraderived gneisses (G1 Supersuite and Nova Venécia	Unknown	-10.49 ~ -9.28 (gabbro); -11.28 ~ -7.33 (charnockite)	37.43 (gabbro); 29.22 ~ 51.47 (charnockite)

		granite, charnockite	Complex, respectively)			
Conceição de Muqui	50	Monzodiorite, syeno-monzonite, granite	Ortho- to paraderived gneisses (G1 Supersuite and Nova Venécia Complex, respectively	Unknown	Unknown	Unknown
Mimoso do Sul	80	Monzodiorite, syeno-monzonite, granite	Orthogneisses (G1 Supersuite) and paragneisses (Nova Venécia Complex)	498 +- 5 (monzonite)	-14.58 ~ -12.20 (monzonite)	39.89 ~ 41.23 (monzonite)
Jacutinga	14	Gabbro	Orthogneiss (G1 Supersuite)	Unknown	-14.10 ~ -10.39 (gabbro)	45.54 ~ 59.94 (gabbro)
Itaoca	11	Gabbro	Orthogneiss (G1 Supersuite) and marble (Nova Venécia Complex).	Unknown	-8.05 ~ -3.83 (gabbro)	15.31 ~ 30.24 (gabbro)

2.2.1. Afonso Cláudio Intrusive Complex review

The regional mapping projects in Espírito Santo state (Brazil) approached the field relationships, petrography and some lithogeochemical data of the ACIC, earlier named as Afonso Cláudio Intrusive Massif (Silva and Ferrari, 1976; Filho et al., 1983; Féboli et al., 1993; Signorelli et al., 1993; Vieira et al., 1993; Vieira, 2015). Beyond these works, Paradella et al. (1978) investigated the ACIC and others post-collisional plutons from Espírito Santo state by remote sensing.

These works reported that there is a low topographic region in ACIC center where mafic rocks (dioritic and gabbroic compositions) occur surrounded by felsic rocks (granitic and monzonitic compositions) in high hills. The geological contact between these rocks is characterized by a strong topographic contrast. Norite and pyroxene-monzonite were locally mapped. The main host rocks are paragneisses of the Nova Venécia Complex and granitoids of the G1 Supersuite. The geological contact among surrounding and ACIC rocks is abrupt and there are localized intrusions of ACIC felsic rocks into surrounding rocks. In addition, enclaves of host rocks were mapped in the mafic and felsic rocks of the ACIC.

2.3. Analytical methods

The geological mapping was executed at 1:25.000 scale and based on 298 field stations.

A total of 61 thin sections were studied, which 6 represent host rocks and 55 represent ACIC rocks (including mafic enclaves and host rocks xenoliths). The thin sections were made at lamination labs of the Federal University of Minas Gerais, Federal University of Ouro Preto and Federal University of the Espírito Santo and described under transmitted light polarizing microscopes Zeiss Axioskop 40 and Olympus BX-41 at Federal University of Minas Gerais.

Twenty samples were analyzed by whole-rock geochemistry (majors, traces and rare-earth elements - REE) in SGS Geosol labs. Monzogabbro, monzodiorite, quartz monzonite, jotunite and quartz mangerite were analyzed. The samples were washed, dried to 105 ºC, crushed to 3 mm in crusher machine, homogenized, quartered, crushed to 150 mesh in agate ball mill 95% and melted with lithium metaborate. The major elements concentrations were analyzed by Inductively Coupled Plasma Optical Emission Spectroscopy (ICP-OES), while the trace and REE elements concentrations were measured by Inductively Coupled Plasma Mass Spectroscopy (ICP-MS). The LOI was calculated by weight difference after 1000ºC heating. The results were analyzed by software GCDKit (Janoušek et al., 2006). The whole-rock geochemistry results are presented in Supplementary Table 1.

Two lithotypes were selected for obtaining U-Pb ages, the monzogabbro (sample P 246-A) and the quartz monzonite (sample P 98). The zircons from these two samples were separated by conventional techniques including crushing, sieving, magnetic and heavy liquids separation, and handpicked under a binocular microscope. The handpicked selected zircons were mounted in epoxy resin and polished to expose the crystal centers. Cathodoluminescence was performed by Scanning Electronic Microscope (SEM) JEOL JSM 6510 at the Microscopy and Microanalysis Laboratory of the Geology Department of the Federal University of Ouro Preto. The U-Pb isotopic compositions were analyzed by Thermo Scientific Element 2 sector field ICP-MS coupled to a CETAC LSX-213 Nm G2 laser ablation system equipment (SF-LA-ICP-MS) at the Isotope/Geochemistry Laboratory of the Geology Department of the Federal University of Ouro Preto. The primary and secondary standards are shown in Supplementary Table 2 and the full data were processed using Glitter software (Achterbergh et al., 2001). In each sample were made spot analyses with about 20 μm. The concordia and weighted average ages were calculated using Isoplot 4.15 (Ludwig, 2003). Uncertainties given for individual analyses (ratios and ages) are at the 1 sigma level, while the uncertainties in the concordia and

weighted ages are at 2 sigma level. The U-Pb dating results are presented in Supplementary Table 2.

The Lu-Hf analyses were performed at the Isotope/Geochemistry Laboratory of the Geology Department of the Federal University of Ouro Preto using a Thermo-Scientific Neptune Plus multi-collector ICP-MS system coupled to a Photon Machines 193 Nm ArF Excimer laser ablation system (MC-LA-ICP-MS). The samples, zircons and spots analyzed were the same of the U-Pb analyses, however each analyzed spot has about 30-40 μm. The standard zircons used are presented in Supplementary Table 3. The εHf values were obtained using U-Pb ages and T_{DM} was calculated following Chauvel et al. (2008). The Lu-Hf isotopic results are shown in Supplementary Table 3.

2.4. Results

2.4.1. Geological mapping and field relationships

The ACIC is an almost elliptical igneous body slightly elongated in E-W direction, with ca. 73 km², highlighted in geophysical images (Figure 2.2). It is intrusive in garnet-cordierite-sillimanite-biotite gneiss to north and south, garnet-sillimanite-biotite gneiss to northwestern (both paragneisses of the Nova Venécia Complex) and allanite gneiss to east and west (orthogneisses of the G1 Supersuite) (Signorelli et al., 1993; Vieira, 2015). The geological contact between surrounding rocks and ACIC is sharp, marked by topography contrast, while the edge felsic rocks from ACIC occur in high hills, the host rocks occur in smaller hills. The igneous border foliation of the ACIC and host rocks' metamorphic foliation are concordant and there are locally small intrusions of felsic rocks of the ACIC into host rocks. Two dextral shear zones were found on the east and west sides of the ACIC and it is possible to see shear evidences, such as stretched quartz crystals and fragmented feldspar porphyries, in some places in the ACIC edge. Partial melting process can be observed locally. This feature is mainly observed in the paragneisses, which the leucosome is represented by a leucogranite composed mainly of feldspar, quartz and residual biotite.

The ACIC is an inversely zoned pluton, with two off-centered mafic cores composed of monzogabbro and monzodiorite exposed in low topographic regions (Figure 2.3a) and quartz monzonite's high hills surrounding these mafic cores (Figure 2.3a and 2.3b). The geological

contact between mafic and felsic rocks is characterized by a strong topographic contrast. The quartz monzonite represents the prevailing lithotype of the ACIC and magmatic foliation is a common feature of this rock from ACIC edges, marked by the orientation of phenocrysts and biotite crystals.

The mafic cores are mainly composed of monzodiorite (Figure 2.3d and 2.3e). The monzogabbro (Figure 2.3f) is more restricted and sometimes it occurs as enclaves (possible autholiths) in monzodioritic rocks. These rocks are showed as one unit in geological map (Figure 2.2) because outcrops of these rocks are scarce, exposed mainly in riverbeds (Figure 2.3g), and due to these rocks occur associated. At the mafic core near Empossado village occurs a big flat region. This area is covered by a Quaternary deposit and many eroded blocks of the mafic rocks and quartz monzonite (Figure 2.3a).

In all extension, the ACIC rocks are intruded by syenogranite dykes (Figure 2.3d and 2.3h). Quartz veins and quartz-feldspar dykes (frequently pegmatitic and mainly composed of quartz, feldspar and occasional biotite and sometimes carrying minerals as aquamarine, tourmaline and quartz varieties) are also common. Both dykes and veins range in size from centimetric to about one meter thickness.

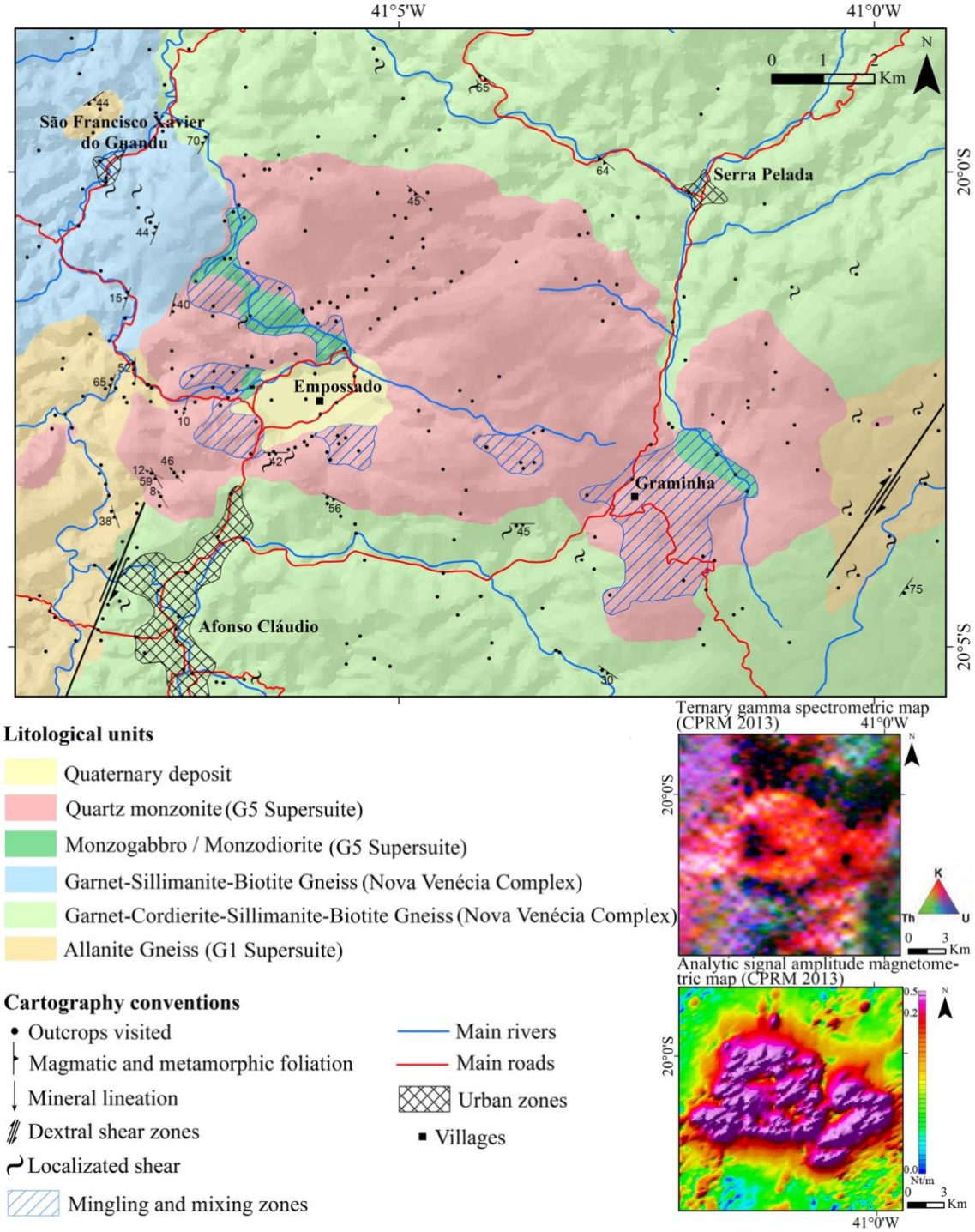

Figure 2.2: Geological map of the Afonso Cláudio Intrusive Complex (1:25.000 scale).

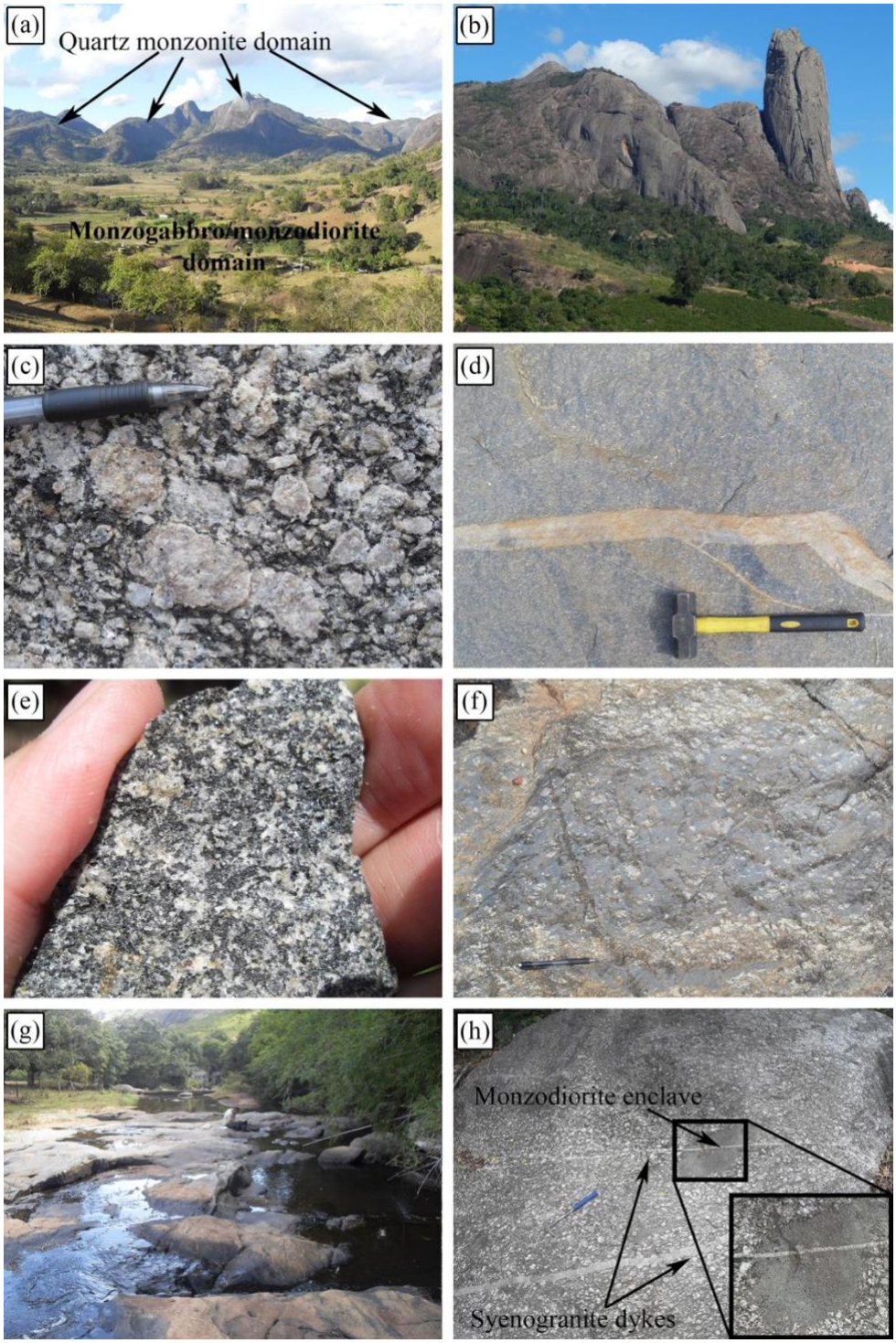

Figure 2.3: Field photos of the ACIC field aspects. (a): Mafic rocks in low topographic region surrounded by quartz monzonite high hills at the Empossado region. (b): Quartz monzonite typical domain in high hills. (c): Quartz monzonite sample in detail. (d): Monzodiorite intruded by a syenogranite dyke. (e): Monzodiorite sample in detail. (f): Monzogabbro enclave enclosed by quartz monzonite. (g): Representative outcrop of the mafic rocks (monzodiorite and monzogabbro). (h): Quartz monzonite outcrop showing a monzodiorite enclave and crossed by syenogranite dykes.

Between the felsic and mafic rocks, mingling and mixing zones were mapped. These zones are evidenced by mafic microgranular enclaves (MME) in quartz monzonite, some of them stretched (Figure 2.4a), K-feldspar and plagioclase xenocrysts from quartz monzonite inside mafic rocks (Figure 4b), sometimes ovals, quartz monzonite net-veined complexes into mafic rocks (Figure 2.4b) and felsic magma injections in mafic rocks (Figure 2.4c). These features were described by Hibbard (1995), Janousek et al. (2000) and De Campos et al. (2016) as evidences of magma mingling and mixing. In the magma mixing and mingling zone at Graminha locality, jotunite (orthopyroxene monzodiorite) and quartz mangerite (orthopyroxene-bearing quartz monzonite) were locally mapped (Figure 2.4d).

Enclaves and xenoliths are common in all ACIC area. The quartz monzonite hosts monzogabbro and monzodiorite enclaves (MME) (Figure 2.3h and 2.4e), ranging in shape from circular/oval (main type) to angular (occasional) and in size from centimeters to about one meter in diameter. The contact of MME with quartz monzonite varies from gradual (mainly on circular MME) to abrupt (mostly on angular MME). Both mafic and felsic rocks incorporate the ACIC host rock xenoliths and the main ones are allanite orthogneisses (Figure 2.4e) and granulitic paragneisses (Figure 2.4f). Besides these, xenoliths of the amphibolite and tonalite (likely rocks of the G1 Supersuite) and calcium silicate rock (likely rock of the Nova Venécia Complex) occur. The xenoliths range in size from centimeters to about one meter in diameter, in shape from circular to angular and the contact with ACIC rocks ranges from abrupt to gradual. The xenoliths with gradual contact apparently show evidence of partial melting, mainly allanite orthogneiss and granulitic paragneiss (Figure 2.4f).

2.4.2. Petrography

The ACIC rocks were classified following the QAPF diagram as monzogabbro, monzodiorite, quartz monzonite, jotunite, quartz mangerite and syenogranite (Figure 2.5 and Table 2.2) (Streckeisen, 1974, 1976 adapted by Le Maitre et al., 2002).

The monzogabbro (ranging to quartz monzogabbro) is a gray color rock (Figure 2.3f) with porphyritic texture and equigranular phaneritic matrix. The size of the phenocrysts ranges normally from 4 mm to 6 mm, and rarely reach 2 cm. The matrix is fine- to medium-grained ranging from 0.125 mm to 3 mm. The major phases are plagioclase, biotite, clinopyroxene and K-feldspar. Quartz, opaque minerals, hornblende (rare), apatite and zircon are the accessory

minerals (Figure 2.6a and 2.6b). Orthopyroxene is occasional. The main secondary minerals are sericite (replacing the plagioclase and K-feldspar) and carbonate (replacing plagioclase, hornblende and pyroxenes). Some plagioclase crystals show compositional zoning and are the main phenocrysts of this rock. K-feldspar porphyries are rare. Pyroxenes are partially replaced by biotite and hornblende, which is also partially transformed in biotite. Rare clinopyroxenes mantled by hornblende occur.

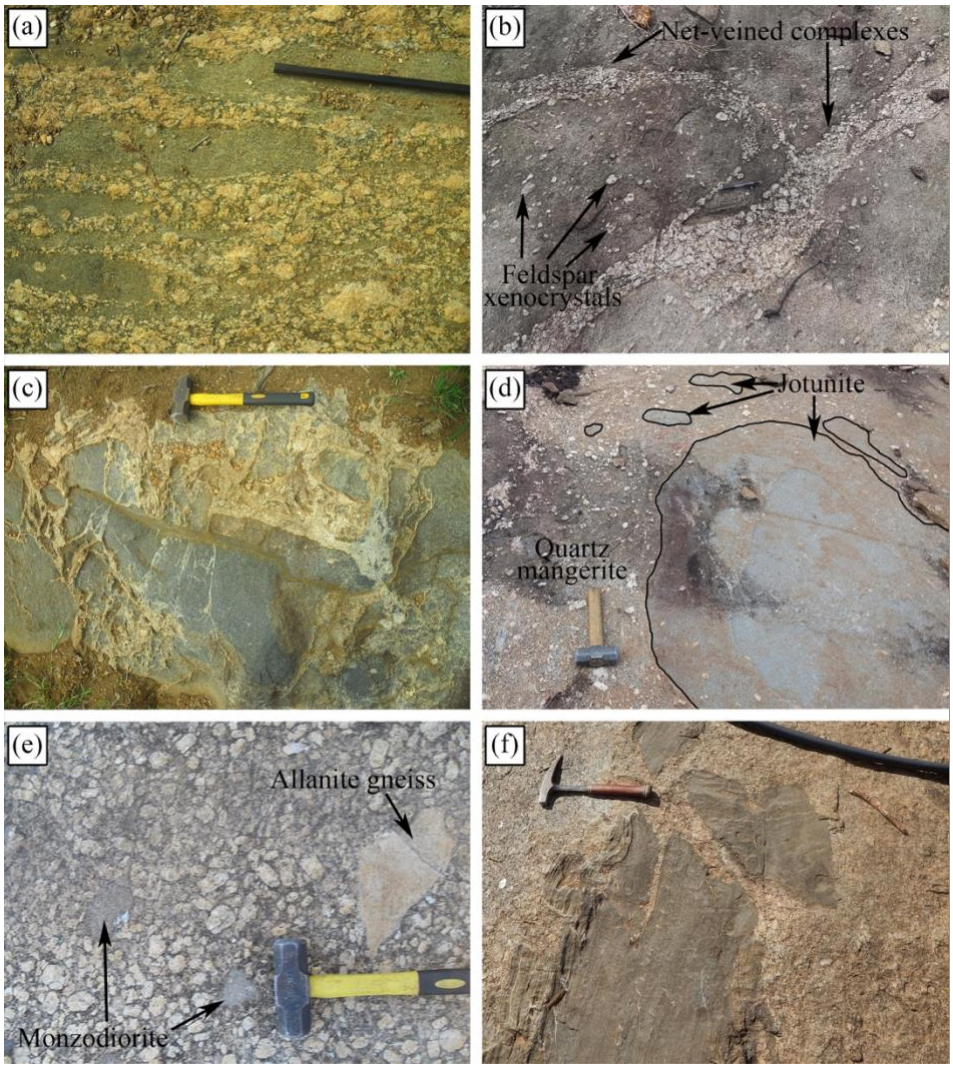

Figure 2.4: Field photos of the ACIC field aspects. (a): Mafic enclaves stretched in the quartz monzonite. (b): Quartz monzonite net-veined complexes crossing mafic rocks and feldspar xenocrysts assimilated by mafic rocks. (c): Felsic magma injections into mafic rocks. (d): Field aspect of the jotunite and quartz mangerite in mingling and mixing zone at Graminha region. (e): Quartz monzonite outcrop containing angular allanite gneiss xenolith and rounded monzodiorite enclave (MME). (f): Granulitic paragneiss xenolith in quartz monzonite domain. The quartz monzonite is apparently assimilating the paragneiss rock.

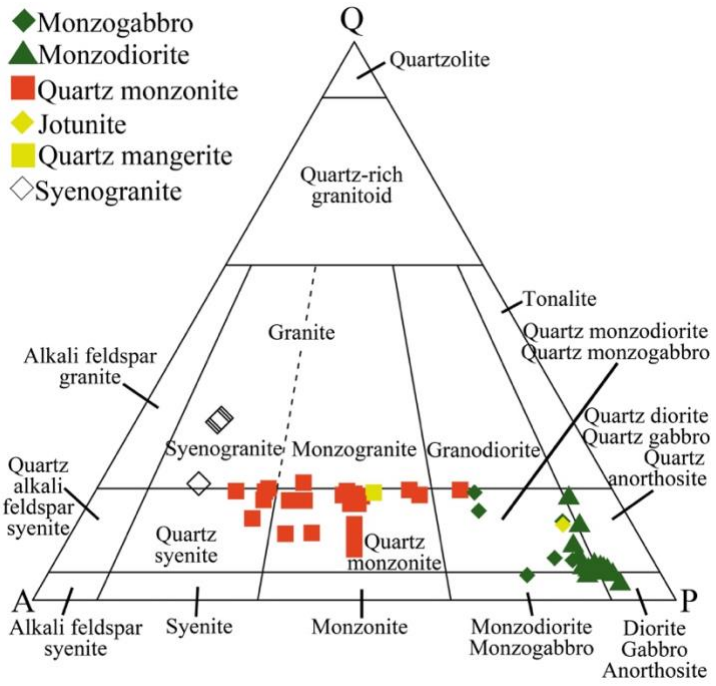

Figure 2.5: ACIC rocks classification by QAPF diagram (Le Maitre et al., 2002 based on Streckeisen, 1976).

The monzodiorite (ranging to quartz monzodiorite and quartz diorite) is a gray rock (lighter than monzogabbro) (Figure 2.3e) with fine- to medium-grained equigranular phaneritic texture (Figure 2.6c) and the crystal size ranges from 0.25 mm to 2.5 mm. There are locally phenocrysts of the up 6 mm size. Plagioclase, biotite, hornblende, clinopyroxene and K-feldspar are the major mineral phases, while quartz, opaque minerals, apatite, titanite and zircon are the accessory minerals. The secondary minerals are sericite (replacing the plagioclase and K-feldspar), carbonate (replacing plagioclase and hornblende) and chlorite (replacing biotite crystals). Some plagioclase crystals show compositional zoning and in the few porphyritic samples they are the main phenocryst. Occasionally K-feldspar phenocrysts occur and rarely show poikilitic texture, with clinopyroxene, opaque minerals and biotite inclusions. Glomeroporphyritic texture rarely occurs, with feldspar, quartz, biotite and clinopyroxene with slightly bigger size than the other minerals. Preserved clinopyroxenes are rare and many of them are partially transformed to biotite and hornblende. Coronitic texture commonly occur, with hornblende surrounding clinopyroxene crystals (Figure 2.6d). Hornblende is occasionally replaced by biotite. Biotite and hornblende commonly have symplectitic intergrowth with quartz and titanite frequently occurs as rim in opaque minerals (magnetite and ilmenite).

Table 2.2: Estimated modal mineralogy of the ACIC lithotypes. The numbers in parenthesis represent the highest modal values of each lithotype.

Lithotype / Mineral	Monzogabbro	Monzodiorite	Quartz monzonite	Jotunite	Quartz mangerite	Sineogranite
Quartz	2 - 4% (12%)	3 - 4% (17%)	(7%) 10 - 17%	10%	16%	19 - 30%
Plagioglase	41 - 58% (64%)	43 - 58%	19 – 57% (43%)	56%	36%	12 - 14%
K-Feldspar	(3%) 7 - 14 % (17%)	1 - 5% (18%)	19 - 43%	4%	31%	50 - 58%
Hornblende	<1 - 2% (18%)	(2%) 8 - 23%	1 - 11%	-	2%	<1 - 2%
Biotite	(3%) 8 - 14% (23%)	(4%) 10 - 32%	4 - 14%	10%	6%	<1 - 2%
Orthopyroxene	(1%) 3 - 7%	-	-	4%	<1%	-
Clinopyroxene	(1%) 8 - 18%	1 - 15%	-	8%	<1%	-
Titanite	-	<1 - 3%	0 - 3%	-	<1%	<1 - 1%
Zircon	<1 - 1%	<1 - 1%	<1 - 1%	<1%	<1%	<1 - 1%
Allanite	-	-	<1 - 1%	-	<1%	1%
Opaque minerals	2 - 5%	1 - 4%	<1 - 3%	4%	2%	1 - 2%
Apatite	<1 - 1%	1 - 2%	<1 - 1%	1%	1%	<1 - 1%
Sericite	<1 - 1%	<1 - 2%	<1 - 2%	1%	1%	1 - 3%
Carbonate	<1 - 1%	<1 - 1%	<1 - 2%	1%	1%	<1 - 1%
Chlorite	-	<1 - 1%	< 1% - 1%	-	<1%	<1 - 2%
Muscovite	-	-	<1 - 1 %	-	-	-

The quartz monzonite has fine- to coarse-grained phaneritic matrix, ranging from 0.5 mm to 4 mm, and porphyritic texture (Figure 2.6e). The porphyry size ranges from 4 mm to 4 cm. The major mineral phases are microcline, plagioclase, quartz, biotite and hornblende. Opaque minerals, titanite, apatite, allanite and zircon are minor mineral phases. Sericite (replacing microcline and plagioclase), carbonate (replacing plagioclase and hornblende), chlorite (replacing biotite and hornblende) and rare muscovite (it is apparently replacing the feldspar crystals) are the secondary minerals. The main and biggest phenocrysts are microcline crystals, which sometimes show poikilitic texture, with mainly plagioclase inclusions (Figure 2.6f). Plagioclase phenocrysts commonly occur and many plagioclase crystals show

compositional zoning. Larger xenomorphic quartz crystals than matrix grains occasionally occur, reaching up 3 centimeters. The hornblende is also replaced by biotite, that sometimes surrounds hornblende crystals. Hornblende and biotite have quartz symplectitic texture. Opaque minerals (magnetite and ilmenite) commonly occur surrounded by titanite (coronitic texture).

These three lithotypes have common features. The feldspar phenocrysts are hypdiomorfic and idiomorfic and they are occasionally fractured, with the fractures filled by quartz and carbonate. Feldspar crystals in matrix also present this feature. In some samples, quartz and feldspar show some deformational evidences, as undulose extinction, subgrains, polygonal grain boundaries and curved polysynthetic twinning. Rare stretched quartz crystals also occur in the quartz monzonite. The K-feldspar is normally perthitic in these rocks (in monzodiorite is rarer) and occasional antiperthitic plagioclase occur in mafic rocks. When K-feldspar and plagioclase are in contact, myrmekite is commonly generated. The rocks within and near the mingling and mixing zones present some acicular apatite crystals, K-feldspar and plagioclase porphyries (xenocrysts), which sometimes show oval and corroded terminations, and rapakivi and anti-rapakivi textures.

The syenogranite dykes are grey to white with fine- to medium-grained equigranular phaneritic texture and the crystal size ranges from 0.25 mm to 2.5 mm. Microcline, quartz and plagioclase are the major mineral phases (Figure 2.6g). Opaque minerals, biotite, hornblende, zircon, allanite, apatite and titanite are minor mineral phases. The secondary minerals are sericite (replacing feldspar crystals), carbonate (replacing plagioclase crystals), and chlorite (replacing biotite and rarely hornblende). Many microcline crystals are perthitic and myrmekite is generated when these ones are in contact with plagioclase. Biotite crystals occasionally occur replacing hornblende.

The quartz mangerite is a porphyritic rock with fine- to medium-grained equigranular phaneritic matrix. The size of porphyritic crystals ranges from 4 mm to 1.25 cm, while the size of matrix crystals ranges from 0.125 mm to 4 mm. The major mineral phases are plagioclase, microcline, quartz and biotite. Hornblende, opaque minerals, orthopyroxene, clinopyroxene, titanite, apatite, zircon and allanite are the minor mineral phases. The secondary minerals are sericite (replacing feldspar crystals), carbonate (replacing plagioclase and hornblende) and chlorite (replacing biotite and clinopyroxene). The main porphyries are plagioclase and microcline crystals, which rarely seem to show a slight orientation. The clinopyroxene is partially replaced by hornblende, which sometimes surrounds clinopyroxene crystals, while the biotite crystals are replacing hornblende. Some apatite crystals are acicular.

Jotunite is an equigranular phaneritic fine- to medium-grained rock locally porphyritic, the size of the crystals ranges from 0.25 mm to 1.5 mm. The size of the rare porphyries varies between 4 mm and 5 mm. Plagioclase, quartz, biotite, K-feldspar and clinopyroxene are major mineral phases. Opaque minerals, orthopyroxene, apatite and zircon are accessory minerals. Carbonate (replacing plagioclase and pyroxenes) and sericite (replacing the K-feldspar crystals) are the secondary minerals. The rare phenocrysts are plagioclase. The hypidiomorfic and idiomorfic biotite crystals are slightly larger than rock average matrix, reaching 1.5 mm (Figure 2.6h). Some apatite crystals show acicular texture.

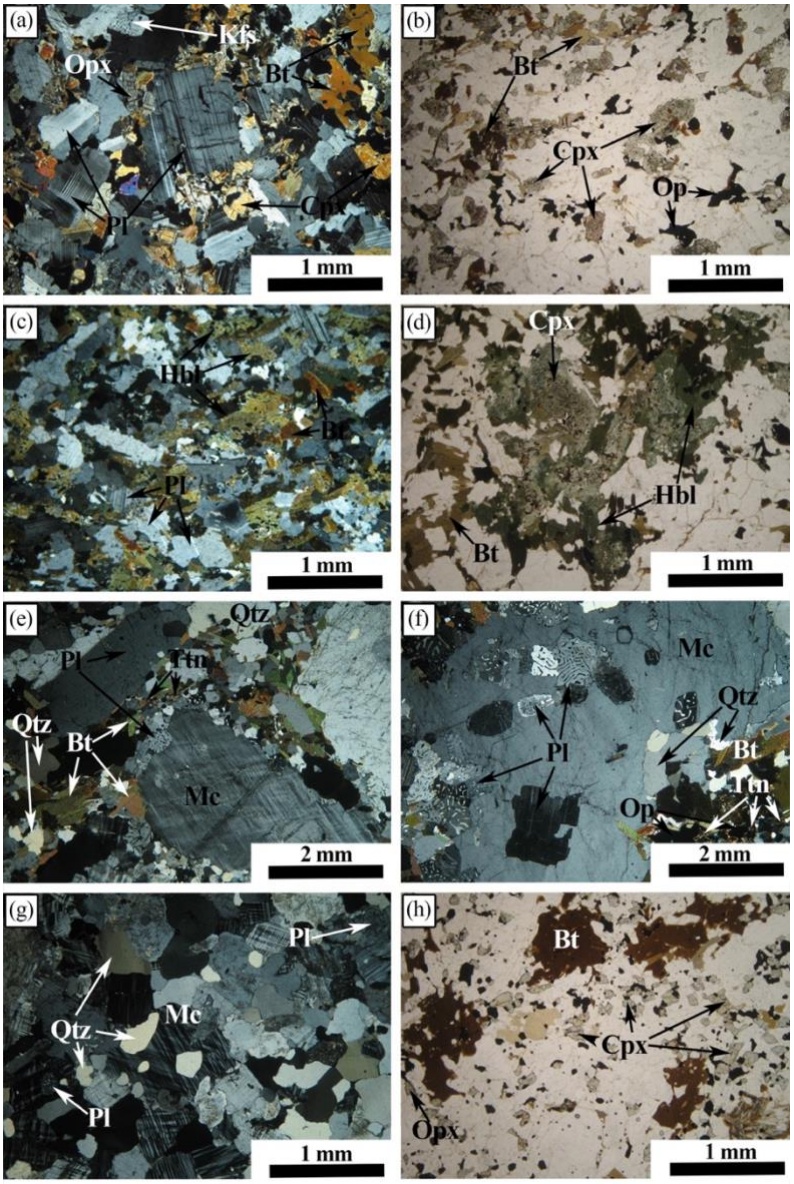

Figure 2.6: Photomicrographs of the ACIC rocks. (a) and (b): General texture and mineralogy of the monzogabbro (a is under plane polarized light and b is under crossed polarized light). (c): General texture and mineralogy of the monzodiorite (crossed polarized light). (d): Hornblende crystals surrounding clinopyroxene with coronitic texture (crossed polarized light). (e): Porphyritic texture and general mineralogy of the quartz monzonite (crossed polarized light). (f): Poikilitic texture in microcline phenocrysts of the quartz monzonite with many plagioclase inclusions (crossed polarized light). (g): General texture and mineralogy of the syenogranite dykes (crossed polarized light). (h): General texture and mineralogy of the jotunite; biotite crystals are bigger than general matrix (plane polarized light). Mineral abbreviations are: Bt: Biotite; Cpx: Clinopyroxene; Hbl: Hornblende; Kfs: K-feldspar; Mc: Microcline; Op: Opaque mineral; Opx: Orthopyroxene; Pl: Plagioclase; Qtz: Quartz; Ttn: Titanite.

2.4.3. Whole-rock geochemistry

The silica content of the ACIC rocks ranges from 49 wt% in monzogabbro to 69 wt% in quartz monzonite and the alkalis content ranges from 5 wt% in mafic rocks to 10 wt% in the quartz monzonite. The rocks were classified as monzogabbro, monzodiorite, monzonite and quartz monzonite in TAS diagram (Figure 2.7a), in agreement with their petrographic classification in the QAPF diagram (Figure 2.5).

Monzogabbro and monzodiorite show higher values of TiO_2, FeO_t, MnO, MgO, CaO, P_2O_5, Ni, Sr, Nb and Co than quartz monzonite. The quartz monzonite is enriched in K_2O, Ba, Rb, U and Th when compared with mafic rocks. Al_2O_3, Na_2O, Zr, Hf and Y are scattered in the samples. The jotunite and quartz mangerite show intermediary values of these elements, positioning them between the mafic and felsic groups (Figure 2.8).

There are positive linear trends between SiO_2, K_2O, Ba, Rb, U and Th from mafic to felsic rocks, whereas TiO_2, FeO_t, MnO, MgO, CaO, P_2O_5, Ni, Sr, Nb and Co show negative linear trends (Figure 2.8).

The ACIC rocks are metaluminous with A/CNK [molar $Al_2O_3/(CaO+Na_2O+K_2O)$] varying from 0.6 to 1 (Figure 2.7b). In AFM diagram, the samples plot between calc-alkaline and tholeiitic field limits (Figure 2.7c). Otherwise, the rocks belong to an alkali-calcic series if considering the relationship between alkalis, CaO and SiO_2 (Figure 2.7d), while the K_2O/SiO_2 diagram reveals an affinity with a shoshonitic series (Figure 2.8). The quartz monzonite shows a ferroan signature (Figure 2.9a) and plot between I and A-type granitoids (most of them plot in A-type granite fields) in some granitoid discrimination diagrams (Figure 2.9a, 2.9b, 2.9c and 2.9d). Furthermore, these rocks show geotectonic signature of post-collisional granitoids (Figure 2.9d).

The diagram of REE normalized to chondrite shows a general enrichment in all REE (La/Yb_N =21.45-59.71), with a relative enrichment in LREE when compared to HREE (Figure 2.9e). In general, the analyzed rocks show similar REE patterns, only one quartz monzonite sample deviated from the average pattern. The LREE are more fractioned than HREE (La/Sm_N and Gd/Yb_N = 3.86-6.33 ad 3.57-4.33, respectively). The REE in quartz monzonite (La/Yb_N =21.45-59.71) are slightly more fractioned than in mafic rocks (La/Yb_N =21.84-29.68). There are some small negative Eu anomalies (average Eu/Eu^*_N= 0.801), which are stronger in felsic rocks (average Eu/Eu^*_N= 0.787) than in mafic rocks (average Eu/Eu^*_N=0.803). In the multi-elementary diagram of trace elements normalized to primitive mantle, the samples show similar

pattern and occur an enrichment in LILE if compared to HFSE (Figure 9f). There are negative anomalies of the Ta, Sr, P, Zr and Ti. The Ta, P and Ti more evident negative anomalies in quartz monzonite are due to lower content of such elements in this rock.

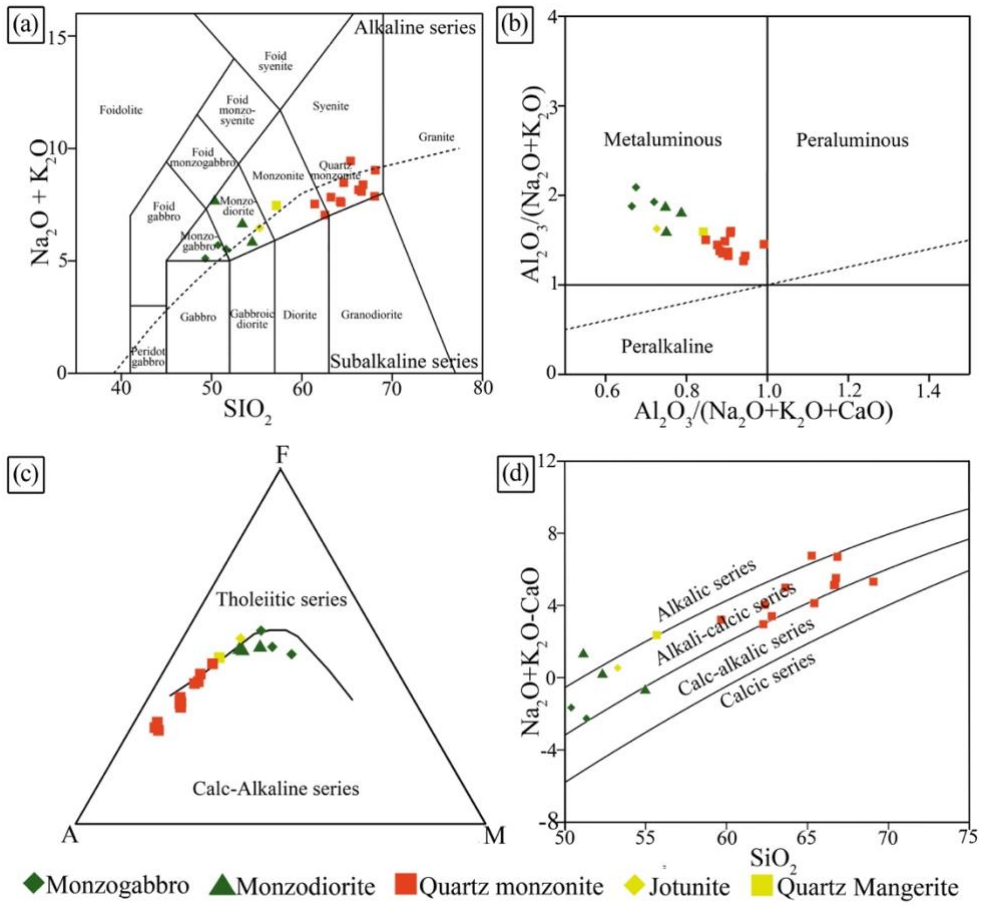

Figure 2.7: Geochemical analyses of the ACIC rocks. (a): $Na_2O + K_2O$ versus SiO_2 (wt%) diagram and its geochemical classification (Le Bas et al., 1986 adapted by Middlemost, 1994). (b): Molar A/NK vs. A/CNK diagram (Shand, 1943). (c): AFM (A = $Na_2O + K_2O$, F = FeO_t, M = MgO) diagram (Irvine and Baragar, 1971). (d): $Na_2O + K_2O$ - CaO versus SiO_2 (wt%) diagram segmented by series based on alkalis content (Frost et al., 2001).

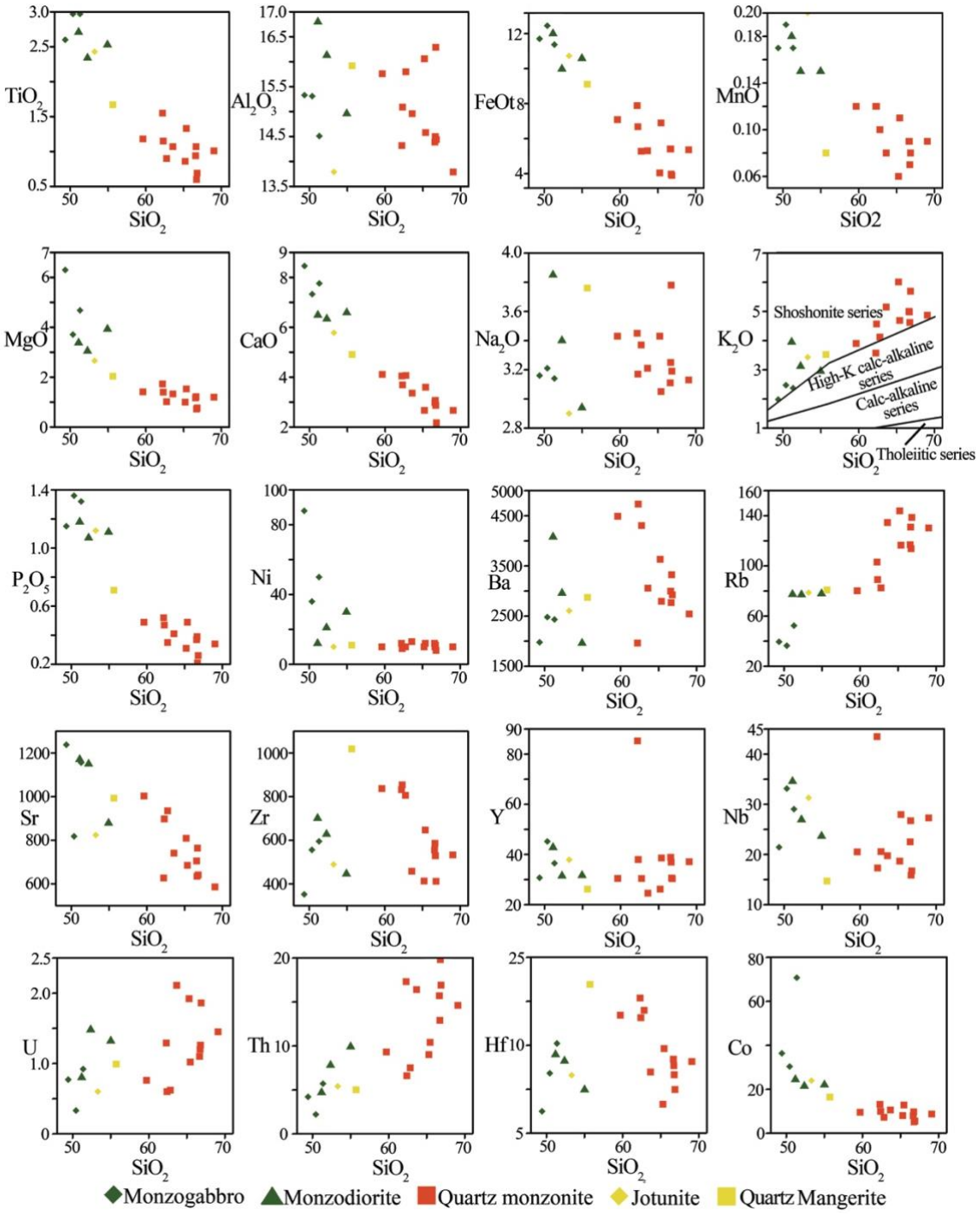

Figure 2.8: Binary diagrams (Harker diagrams) from ACIC rocks (major and trace elements versus silica content) (Harker, 1956). K_2O versus SiO_2 diagram fields are from Peccerillo and Taylor (1976). Major elements in wt% and trace elements in ppm.

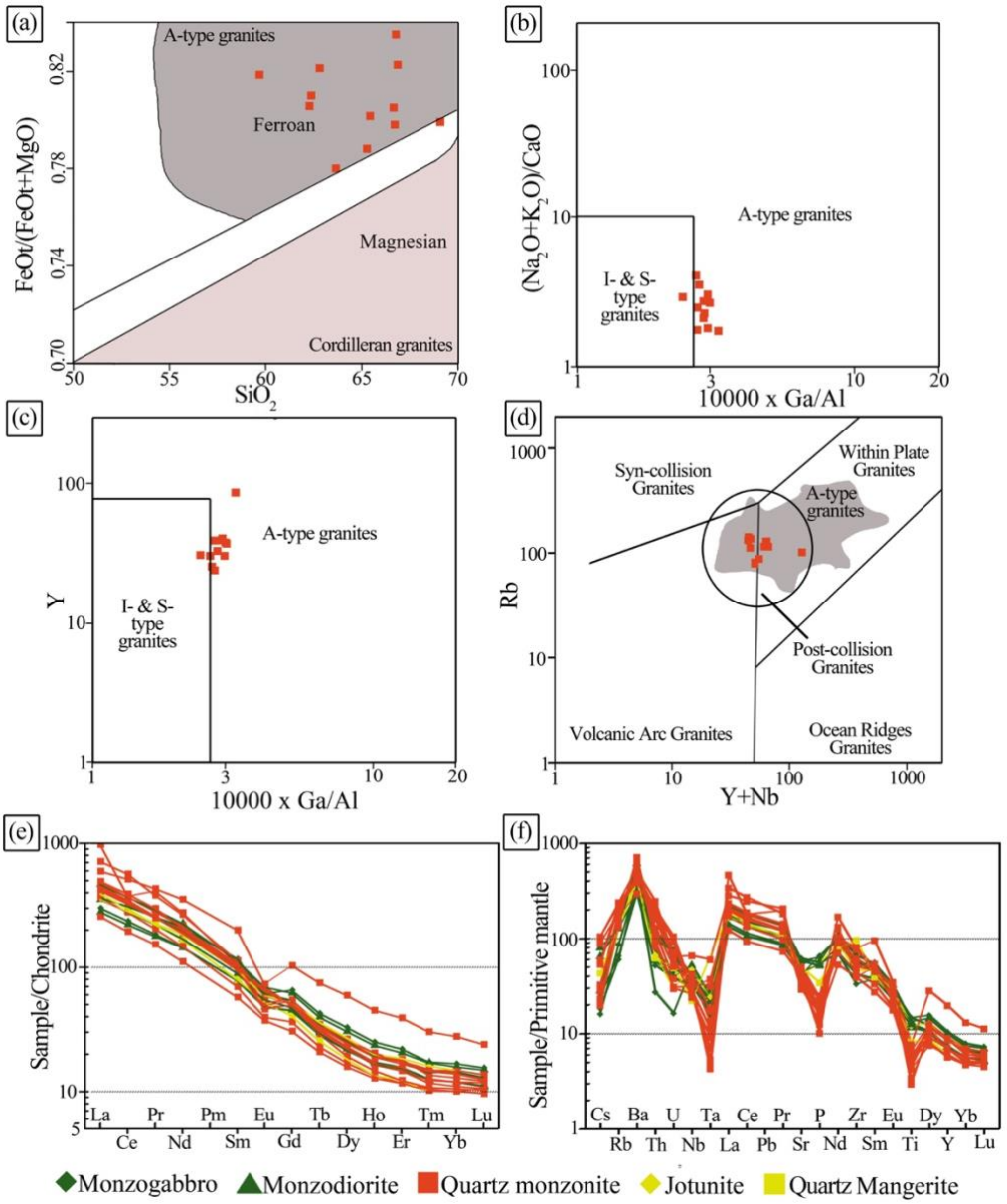

Figure 2.9: Geochemical analyses of ACIC rocks. (a): FeOt/(FeOt +MgO) vs. SiO2 (wt%) diagram, showing the ferroan and magnesian chemical signature and A-Type affinity of granitoids (Frost et al., 2001). (b) and (c): Chemical discrimination diagrams of granitoids (Whalen et al., 1987). (d): Geotectonic classification diagram for granitic rocks (Pearce et al., 1984). (e): Diagram of REE normalized to chondrite (Boynton, 1984). (f): Multi-elementary diagram of trace elements normalized to primitive mantle (McDonough and Sun, 1995).

2.4.4. U-Pb geochronology

The quartz monzonite zircons are colorless, short to long prismatic grains with rounded to subrounded or subhedral to euhedral terminations. The length of the zircon crystals ranges from 90 to 450 µm and width ranges from 50 to 120 µm (the average length/width ratio is 3/1 to 4/1). In cathodoluminescence images, the oscillatory zoning is very clear and most zircons show one evolution core, zircon crystals with two cores are rare. The Th/U ratios range from 0.7 to 3, but one grain shows a Th/U ratio of 4.2. The oscillatory zoning and Th/U ratios point to a magmatic origin of the quartz monzonite. The most of the analyzed zircons show U-Pb concordant ages, only five grains showed older ages than 485 Ma. The quartz monzonite yielded a concordia age of 480.9 ± 3.2 Ma (MSWD=1.03, N=5) and a weighted average age of 480.4 ± 3.4 Ma (MSWD=0.097, N=5) (Figure 2.10).

The zircon grains from monzogabbro are a bit different when compared with zircons from quartz monzonite. The crystals are colorless, apparently broken prismatic grains similar to crystal shards. Very few grains are short perfect prismatic grains. The crystal shards have rounded to sub-rounded or subhedral to euhedral terminations. The length of the zircons ranges from 50 to 250 µm and width ranges from 50 to 150 µm (the average length/width ratio is 2/1). In cathodoluminescence images, the oscillatory zoning in monzogabbro zircon grains is revealed, but it is less clear than the oscillatory zoning in quartz monzonite zircon crystals. The Th/U ratios range from 2.4 to 5.5 with two grains showing Th/U ratios next to 6. These features confirm the magmatic origin of the zircon grains from the monzogabbro. Almost all analyzed zircons show U-Pb concordant ages, just four crystals show older ages than 500 Ma. The concordia age is 496.5 ± 3.6 Ma (MSWD = 1.8, N=5) and the weighted average age is 495.7 ± 3.8 Ma (MSWD = 0.37, N=5) (Figure 2.10).

The concordia and weighted ages in quartz monzonite and monzogabbro zircon crystals were interpreted as magmatic crystallization ages.

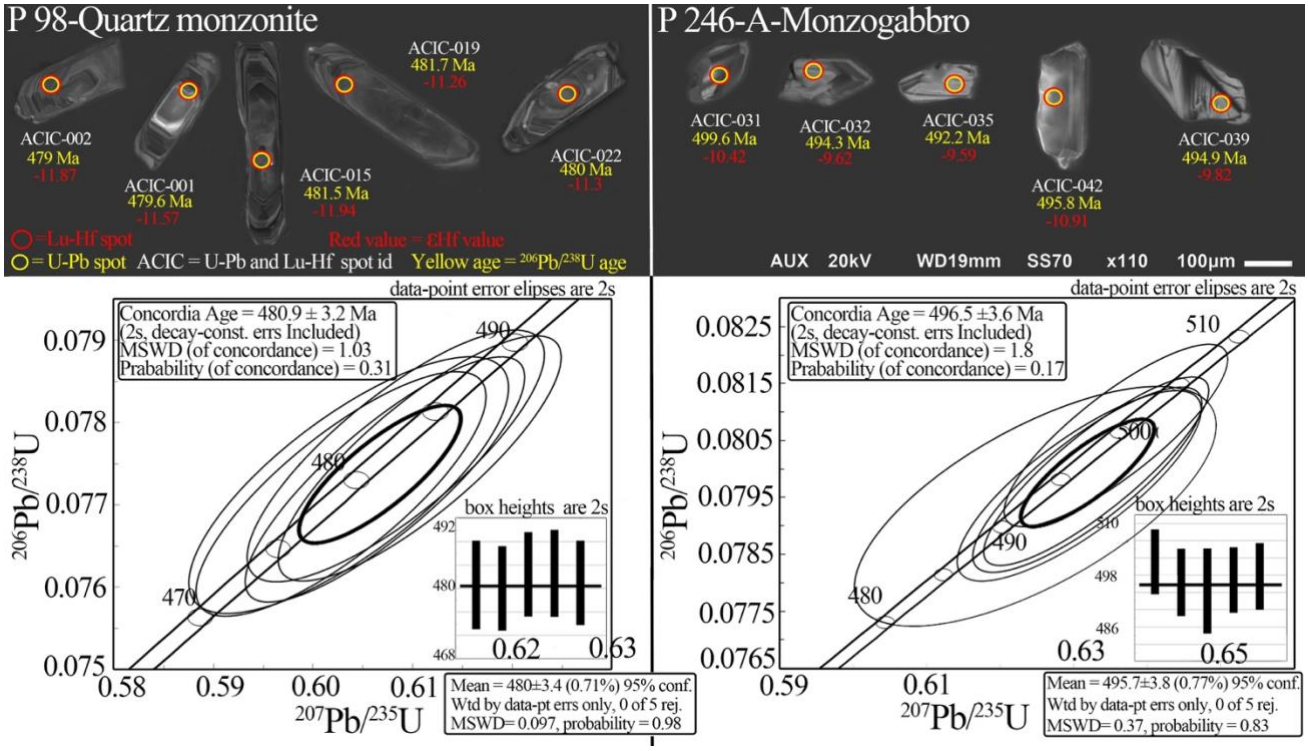

Figure 2.10: Cathodoluminescence images from zircon grains and concordia and mean ages of the quartz monzonite (sample P98) and monzogabbro (sample P 246-A).

2.4.5. Hf isotopes

The quartz monzonite (P98) and monzogabbro (P 246-A) have similar initial $^{176}Hf/^{177}Hf$ ratios. While in the quartz monzonite these ratios range from 0.28212 to 0.28218, these ones in the monzogabbro vary between 0.28213 and 0.28220. Monzogabbro εHf values are between -11.89 and -8.84 (the average value of εHf is -10.41), while in the quartz monzonite these values are ranging from -12.93 to -10.66 (the average value of εHf is -11.78). The T_{DM} ages are slightly close, the quartz monzonite shows T_{DM} ages of 1.73-1.84 Ga (the average T_{DM} age is 1.79 Ga), while the monzogabbro T_{DM} ages are between 1.67 to 1.81 Ga (the average T_{DM} age is 1.72 Ga) (Figure 2.11).

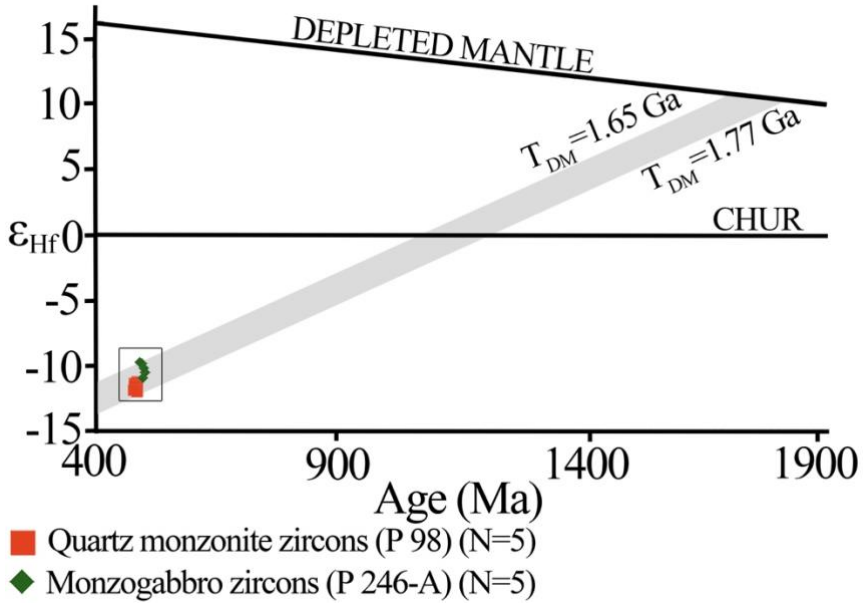

Figure 2.11: εHf versus U/Pb ages of the quartz monzonite and monzogabbro zircons from ACIC.

2.5. Discussion

The main collisional event in the AWCO lasted from 580 to 540 Ma, in this stage the metamorphic grade increased up to granulite facies and older structures were partially overprinted, subsequent thrusting and folding caused crustal thickening (Pedrosa-Soares et al., 2008, 2011; Gradim et al., 2014; De Campos et al., 2016). In the studied area, the lithologic components affected by this stage were granulitic paragneisses of the Nova Venécia Complex (garnet-sillimanite-biotite gneiss and garnet-cordierite-sillimanite-biotite gneiss) and orthogneisses of the G1 Supersuite (allanite gneiss).

During the subduction stage, which precedes the collisional stage, the mantle could have been contaminated by crustal material due to plate subduction and related metasomatism. The plate subduction was probably the main mechanism of mantle contamination until late collisional stage. In figure 2.9f, Ta-Nb negative anomalies in ACIC rocks are typical of subduction setting. This process would have enriched a depleted mantle in incompatible elements as LREE, Ba and Sr. However, these values in G5 rocks are high to be explained only by contamination related to subduction. In addition, the εNd values of about -10 of some basic rocks from G5 plutons need additional source of enrichment to achieve these values (see Table

2.1) (Ludka et al., 1998; Ludka and Wiedemann-Leonardos, 2000; Peixoto et al., 2015; De Campos et al., 2016).

The collapse stage of the AWCO lasted from 530 to 480 Ma. The crustal thickening developed until the end of the collisional stage could be one of the triggers to begin the collapse stage. Decompression in lower crust and lithospheric mantle caused the melting and produced late to post-collisional granitoids (G4 and G5 Supersuites). In this stage, deep faults with predominantly dextral component were generated and played important role to emplacement of the post-collisional plutons in the AWCO, acting as channels for these plutons to ascend to the crust (Figure 2.12) (Pedrosa-Soares and Wiedemann-Leonardos, 2000; Wiedemann et al., 2002; Alkmim et al., 2006).

The intense magmatism in the AWCO during collapse stage may be explained by two main reasons. The slab-break off in the later collisional stage could be one of the reasons. This process would have been responsible for the heat flow and delamination process in lower crust. The delamination process may have caused additional mantle contamination by lower crust material and magma generation (Wiedemann et al., 2002; De Campos et al., 2016). The existence of an active mantle plume, or hotspot onset, could also be a heat and magma source and an engine to the collapse of the orogen, changing the kinematic conditions, from convergent in collisional stage to divergent in collapse stage (De Campos et al., 2016; Serrano et al., 2018). Both processes must have triggered a mantle destabilization and the onset of the post collisional magmatism in the AWCO.

The εNd values in G5 Supersuite range from -14 to -5 (see Table 2.1). This range may be explained by the different country rocks, crustal levels and contamination intensity in each pluton. Late deeper mantle magmas inputs were registered in some plutons as Santa Angélica Intrusive Complex (Zanon et al., 2015), this could have turned the εNd signature of some G5 mafic rocks less negative (De Campos et al., 2016).

The ACIC can be classified as a G5 pluton of the AWCO, since its field aspects, petrography features (igneous fabric preserved), lithogeochemical signature (post-collisional geotectonic signature with I and A2 type granitoids affinity) and U-Pb ages (concordia ages of the 480.9 Ma to quartz monzonite and 496.5 Ma to monzogabbro) support this.

2.5.1. ACIC magma sources and contamination

The ACIC rocks show an alkali-calcic signature and are enriched in K, Ba, Sr, Rb and LREE. These features are not common in juvenile mantle magmas and therefore some contamination process must have occurred (Sparks, 1986). Several authors have studied AWCO post-collisional magmatism and recorded similar geochemical signature to ACIC rocks (Horn and Weber-Diefenbach, 1987; Ludka et al., 1998; Ludka and Wiedemann-Leonardos, 2000; Pedrosa-Soares and Wiedemann-Leonardos, 2000; Medeiros et al., 2001; Wiedemann et al., 2002; De Campos et al., 2004, 2016; Mendes et al., 2005; Belém, 2014). The G5 Supersuite mafic rocks show geochemical signatures similar to each other and they are related to magmas from an enriched mantle. Nd and Sr isotopes studies have also been focused by these authors and the εNd versus εSr diagrams have recorded a crustal component in post-collisional rocks (Ludka and Wiedemann-Leonardos, 2000; Medeiros et al., 2000; De Campos et al., 2016).

Both mafic and felsic rocks from ACIC show an apparent cogenetic signature in the lithogeochemical diagrams. This geochemical affinity can be explained by two ways: magmatic differentiation by fractional crystallization or interaction between magmas from different sources.

The first hypothesis could be sustained by geochemical similarities among the rocks. The affinities are well visualized in TAS, AFM and Harker diagrams, where there are apparently linear cogenetic trends among the analyzed rocks. The REE and incompatible elements diagrams also reveal an apparent geochemical affinity between these rocks. However, in TAS, AFM and Harker diagrams there are gaps between the felsic and mafic rock groups, it could not support the first hypothesis and be an evidence for the second hypothesis.

Besides that, the first hypothesis is difficult to be sustained due to the existence of mingling and mixing zones between the mafic and felsic rocks. The linear trends noted in some diagrams may be explained by the mixing process, which produces these trends, mainly in Harker diagrams. This supports that there were at least two different magmas, with different temperatures and chemical signatures, in a magmatic chamber (Fourcade and Allegre, 1981; Sparks and Marshall, 1986; Barbarin and Didier, 1992; Hibbard, 1995).

The interaction between different magmas could be a strong reason to the similarities between the magmas, the mafic and felsic rocks would be associated to different sources. The mafic rocks would have come from an enriched mantle source and possibly belonged to a tholeiitic series, evidenced by the variation in FeO_t, MgO and TiO_2 values. The felsic rocks

would be associated to crustal source and they would represent alkali-calcic crustal magmas (Bayer et al., 1987; Medeiros et al., 2001; De Campos et al., 2016). The interaction between these magmas, by mingling and mixing processes, would have produced similar geochemical patterns.

The negative εHf values of the mafic and felsic rocks of the ACIC are an important and determinant evidence that some crustal contamination process took place. The mafic magmas have the source related to the mantle and usually show positive εHf values (Kinny and Maas, 2003; Vervoort, 2015). It is the opposite of the mafic rocks from ACIC that show negative values. These ones must have been highly contaminated by crustal material during magma emplacement and ascension, in addition to the previous metasomatism. The contamination by crustal material in G5 plutons have been widely evidenced by previous studies, and it could have enriched the depleted mantle in elements, such as K, Rb, Ba, Sr and LREE, and turned the mafic rocks to negative εNd and εHf values.

Due to the similarities among post-collisional plutons from AWCO, it is possible to suppose that other plutons probably have negative εHf values and it reinforces crustal contamination in the G5 Supersuite plutons.

Many enclaves and host rock xenoliths are found hosted by quartz monzonite, monzodiorite and monzogabbro from ACIC (Figure 2.3h, 2.4e and 2.4f). The host rocks xenoliths occur widespread in all ACIC main rocks, sometimes showing melting evidences (Figure 2.4f). This is a strong evidence that both felsic and mafic igneous rocks assimilated crustal material from host rocks. The paragneisses of the Nova Venécia Complex and allanite orthogneisses of the G1 Supersuite are the main host rock xenoliths in ACIC. Between them, paragneisses are the main ACIC host rock and we believe that this geological unit had an important role in contamination due to its partial melting during the orogenic collapse stage.

The paragneisses of the Nova Venécia Complex have high LREE, alkalis, Al_2O_3, FeO_t and MgO values (Gradim et al., 2014; Richter et al., 2016). But if these rocks were the only sources from felsic magmas, the ACIC rocks would have high Al_2O_3, FeO_t and MgO. Other magma source would be necessary to lower the contents of these elements in the ACIC rocks. The Rio Doce and Rio Negro Arcs are ones of the candidates to sedimentary source of the Nova Venécia Complex (Richter et al., 2016), and could also have contributed to one of the magma contamination sources of the ACIC.

Although of minor occurrence in the studied area, the orthogneiss of the G1 Supersuite may have contributed to the magma and contamination source of the ACIC. The G1 Supersuite

orthogneisses, in the studied area, show low values of the MgO and FeO_t, moderate values of the Al_2O_3 and moderate to high alkalis values (Zanon et al., 2015). A crustal melting involving paragneisses of the Nova Venécia Complex and orthogneisses of the G1 Supersuite could have generated magmas with geochemical signature similar of the ACIC felsic rocks, with high alkalis values, relative low MgO and FeO_t values and enriched in LILE (Ba, Rb and Sr) and LREE.

It is here suggested that there were at least two different magmas involved in evolution of the ACIC. The mafic magmas are associated to a contaminated mantle source due to previous subduction and possibly were contaminated by felsic crustal magmas from different sources during its rising and emplacement.

2.5.2. ACIC petrogenesis

The field aspects, petrography, lithogeochemistry, zircon U-Pb geochronology and Lu-Hf isotopes revealed important igneous processes that acted in the ACIC and contributed to modulate two petrogenetic models for the ACIC.

Deep faulting related to the extensional forces during the orogenic collapse, the associated decompression and increased heat influx may explain lower crust and mantle melting (Pedrosa-Soares and Wiedemann-Leonardos, 2000; Wiedemann et al., 2002; De Campos et al., 2004, 2016; Alkmim et al., 2006; Pedrosa-Soares et al., 2011), which are responsible for felsic and mafic magmas generation, respectively. These faults had a transtensional component, represented by dextral shear zones in the surface, and were the channels used by magmas to ascend to higher crustal levels. This might explain the low shear strain observed mainly in the ACIC edges, which may be an evidence that the end of the AWCO post-collisional state was coeval with the end of the regional shear deformation.

Based on the presented data, two petrogenetic models may be proposed. In both models contamination/assimilation by crustal material and fractional crystallization are involved (AFC processes) and syenogranitic dykes, quartz-feldspar dykes, and quartz veins intruded ACIC in the end of the pluton development, mainly filling the fractures.

2.5.2.1. Model A

In a confined magmatic chamber, installed in a transtentional region, the mafic magma mixed and assimilated a huge amount of crustal material, which includes magmas and host rock xenoliths (Figure 2.12a1), imprinting an alkali-calcic signature in the mafic magma and became this one enriched in LREE and LILE elements, such as Ba, Rb and Sr. Magmatic differentiation processes took place as an AFC process (assimilation and fractional crystallization). The first member crystallized was the monzogabbro, representing the older age obtained for ACIC rocks (ca. 496 Ma). The crustal signature of this rock is attested by enrichment in LILE and LREE and negative εHf values (the average εHf value is -10.41). Subsequently, monzodiorite was crystalized from this mafic magma (Figure 2.12a2).

The monzodiorite and monzogabbro show a strong affinity since their petrography and geochemical signatures are very similar. There are evidences of mineral destabilization in the monzodiorite, as clinopyroxene crystals surrounded by hornblende and hornblende surrounded by biotite (Hibbard, 1995). This destabilization may have occurred during the fractional crystallization.

The AWCO collapse stage would have continued and more extensional stresses acted. In the ACIC magmatic chamber, monzogabbro, monzodiorite (both crystalized rocks) and residual magma coexisted (Figure 2.12a3). With the new extensional stresses, due to the continuity of the collapse stage, the recently crystallized mafic rocks partially melted and produced a new magma (Figure 2.12a4). During this stage, more host rocks also melted. This new magma assimilated more crustal material and became a monzonitic magma richer in alkalis, LILE and LREE than mafic magma.

The monzonitic magma continued the AFC process and generated quartz monzonite at ca. 480 Ma (Figure 2.12a5). The stronger crustal affinity is revealed by higher LILE and LREE values and more negative εHf values (the average εHf value is -11.78) than mafic rocks. The similar whole-rock geochemistry signature, T_{DM} values (average values are 1.79 Ga to quartz monzonite and 1.72 Ga to monzogabbro) and the similar εHf values point to genetic relationship between mafic and felsic magmas. The small differences between the T_{DMs} may be explained by different source contributions to ACIC and the different levels of contamination for country rocks. The oldest zircons from quartz monzonite (older than 485 Ma) could represent inherited zircons from the mafic rocks, but for this interpretation a more robust U-Pb investigation in the zircons of ACIC rocks is needed.

Both mafic and felsic rocks underwent AFC process, but the most intense contamination/assimilation in the mafic rocks occurred during mantle/lower crust melting stage and initial stages of fractional crystallization while in felsic rocks the contamination was most intense in advanced stages of the fractional crystallization (Figure 2.13).

At the time when there were two coeval magmas in ACIC magmatic chamber (monzograbbroic/monzodioric and monzonitic magmas), these magmas mixed and generated jotunite and quartz mangerite (Figure 2.12a5). These rocks show a geochemical signature ranging between the monzogabbro/monzodiorite and quartz monzonite. These magmas also mingled and generated the mingling zones.

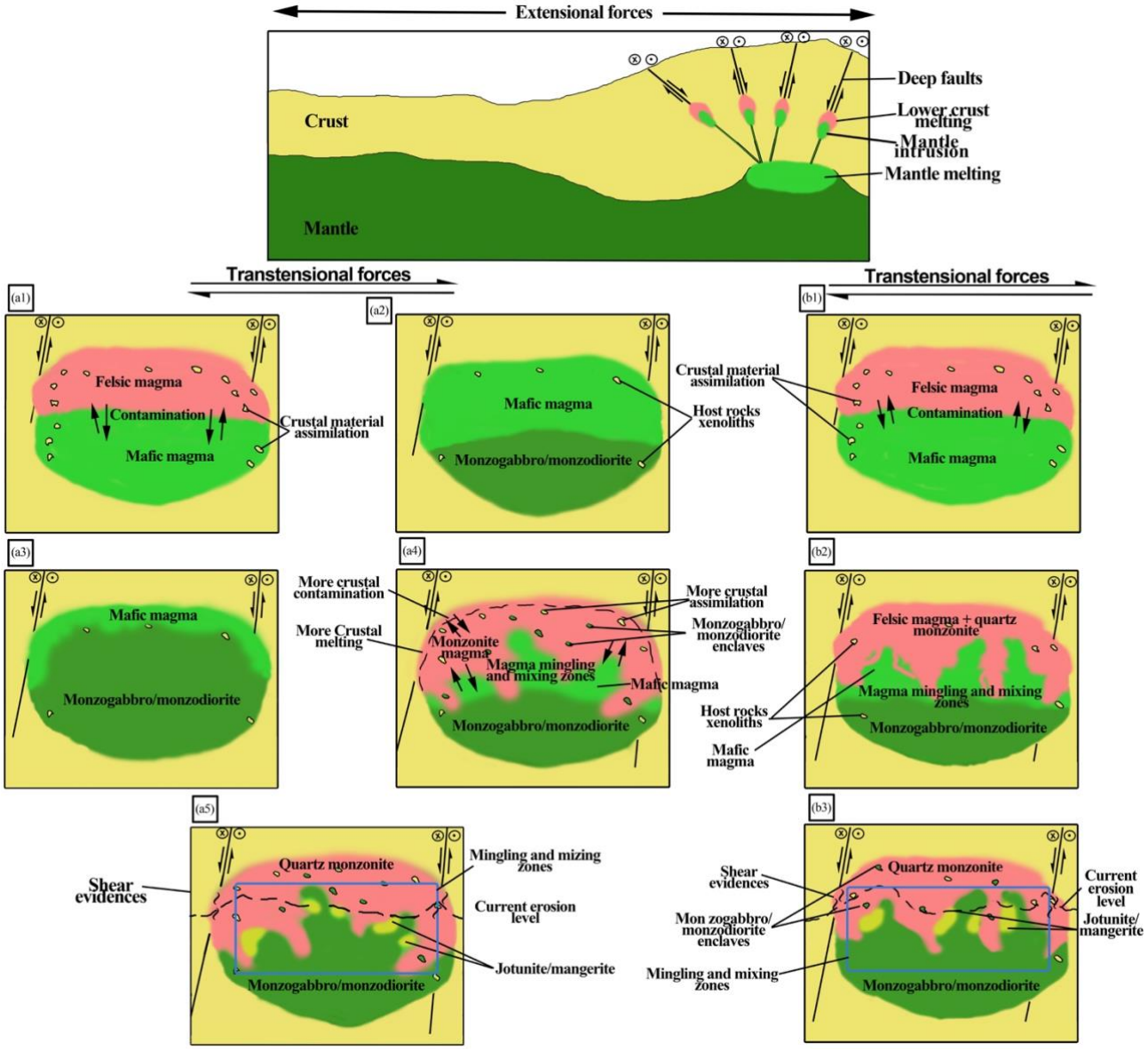

Figure 2.12: Regional setting at the beginning of the Araçuaí-West Congo Orogen collapse stage (upper image) and ACIC schematic petrogenetic models (a and b).

2.5.2.2. Model B

This model follows the one adopted by many authors to explain the post-collisional magmatism in the AWCO (Bayer et al., 1987; Ludka and Wiedemann-Leonardos, 2000; Medeiros et al., 2001; Wiedemann et al., 2002; De Campos et al., 2004, 2016; Mendes et al., 2005).

The first material that filled the magmatic chamber was a felsic magma, which resulted from crustal melting. Subsequently, the mafic magma intruded this magmatic chamber, supporting more crustal melting. This mafic magma was the result of the lithospheric mantle melting and probably assimilated some crustal material during its rising and permanence in the magmatic chamber, where these magmas began an interaction. The mafic magma assimilated more material from felsic magma and both magmas interacted by mixing and mingling processes. During this process, both magmas assimilated more crustal material from the host rocks (Figure 2.12b1).

The magmas acquired some chemical similarities like high LILE and LREE and alkali-calcic signature. The felsic magma has higher values of these elements due to its higher crustal affinity. The εHf values of the quartz monzonite and monzogabbro became negative and similar (the respective average values are -11.78 and -10.41). These similarities may be explained due to mixing process and the isotopic equilibrium between magmas. The similar T_{DM} values (average values are 1.79 Ga to quartz monzonite and 1.72 Ga to monzogabbro) could be due to a different and mixed sources and the mixing process (Martins et al., 2004).

During the interaction process, the fractional crystallization occurred in both magmas, featuring an AFC process. The mafic magma first crystallized monzogabbro (ca. 496 Ma) and in sequence the monzodiorite (see the previous model to see the similarities between the mafic rocks). The quartz monzonite was crystallized from coeval felsic magma at ca. 480 Ma (Figure 2.12b2).

At the moment when there were two different magmas in the magmatic chamber, these magmas interacted and formed the jotunite and quartz mangerite (see previous model to see the explanation about the generation of these rocks) and the mingling zones (Figure 2.12b3).

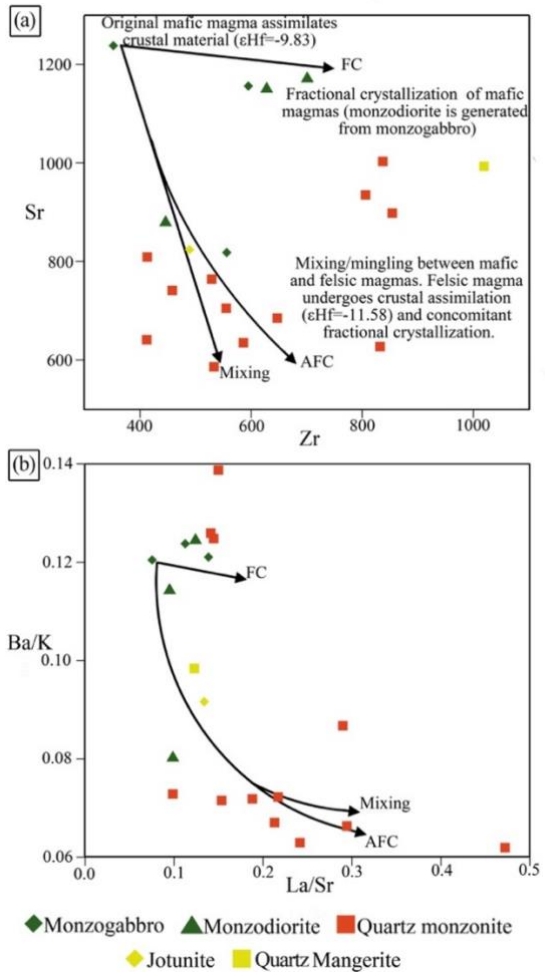

Figure 2.13: Geochemical modeling from ACIC rocks. (a): Sr/Zr and (b): (Ba/K)/(La/Sr) diagrams showing the different igneous process which acted in ACIC. The abbreviations are fractional crystallization process (FC) and assimilation and fractional crystallization process (AFC). The geochemical modeling was made in Microsoft excel spreadsheet program FC-AFC-FCA and MIXING Modeler (Ersoy and Helvaci, 2010; Ersoy, 2013). We considered the initial rock of any igneous process the Si-poorer monzogabbro, which is the most primitive rock in the ACIC. The initial composition of the considered monzogabbro was 48% plagioclase, 18% clinopyroxene, 14% biotite, 7% K-feldspar, 5% quartz, 5% orthopyroxene, 1% hornblende, 1% apatite, 1% opaque minerals and 1% zircon. The relative ratios of assimilated material to crystallized material considered was between 0.6% and 0.8%. The assimilated material considered was the lower continental crust (Taylor and McLennan, 1995).

2.5.3. Discussion about mme origin

MME are found in the quartz monzonite and represent a common feature in granitoids worldwide, being an important tool to uncover magma origins (Barbarin and Didier, 1992). The main hypotheses proposed to MME generation worldwide are: cognate segregation in autholith model, blobs of mantle-derivated magmas model and residues of crustal rocks melting in the restite model (Barbarin and Didier, 1992).

The petrographic characteristics of the MME enclosed by the quartz monzonite are similar to monzogabbro and monzodiorite from ACIC mafic cores (Figures 2.3h and 2.4e) and concerning these MME, although our data about these rocks are scarce, some inferences were possible and we suggest two main hypotheses to these rocks.

If the model A is adopted for explaining the ACIC petrogenesis, the MME could be unmelted residuals or autoliths of the monzogabbro and monzodiorite, which were the precursors of the ACIC felsic rocks. This is evidenced by the similar mineralogy between the MME and the ACIC rocks and the gradual contact between these rocks.

The MMEs could also have formed by blobs of mantle magmas that have mingled and mixed with a felsic magma, following the model B. Some evidences for this are the feldspar xenocrysts in mafic enclaves, some of them showing oval forms, and sharp and wave contacts between the MMEs and its host rocks. All these evidences could suggest the interaction between at least two different magmas (Sparks and Marshall, 1986; Hibbard, 1995; Liu et al., 2013; Sami et al., 2018).

The paleossomes of gneisses partially melted (Figure 2.4f) may be considered crustal restites.

2.6. Conclusions

The ACIC has never been studied in such detailed way and it proved to be one important pluton to better understanding of the post-collisional magmatism in the AWCO. This study showed the ACIC genetical and geological relationship with the AWCO G5 Supersuite. These rocks have been widely studied, however the Lu-Hf analyses are scarce so far and this investigation is one of the first to present Hf isotopes from AWCO post-collisional rocks.

The negative εHf values of the ACIC rocks are a new evidence to crustal contamination in the post-collisional bodies that belong to this orogen, already reported by other authors in post-collisional mafic bodies. Besides that, the alkalis content and relative high LILE (mainly Ba, Rb and Sr) and LREE (mainly in mafic rocks) also evidence the crustal contamination.

Supported on our data, two models could be proposed to ACIC, which may be used to explain others similar post-collisional plutons from AWCO during the collapse stage. Both models are based in AFC process and the deep faults generated in this stage played an important role in the emplacement of these plutons.

The first model argues in favor of an intense interaction between mafic mantle and felsic crustal magmas. These magmas interacted and generated an alkali-calcic mafic magma, which crystallized and formed the monzogabbro and monzodiorite. With the continuation of the collapse stage, these recently crystallized mafic rocks melted and generated a monzonitic magma, which assimilated more crustal material. This new magma crystallized and generated the quartz monzonite.

The second model is similar to the one widely used to explain the G5 Supersuite from AWCO. It argues that the mafic and felsic rocks are from different sources and both magmas were contaminated by themselves and assimilated crustal material, mainly from host rocks. The mantle related mafic magma formed the monzogabbro and monzodiorite, while the felsic crustal magma crystallized the quartz monzonite.

Both models suggest that the jotunite and quartz mangerite were the result of the interaction between the mafic and felsic magmas and the local shear noted in the quartz monzonite may be an evidence that the regional transtensional forces were active until the ACIC cooled and possibly affected other AWCO post-collisional plutons.

3. FINAL REMARKS

This is the first detailed study about the ACIC. In addition, it is one of the first investigations to show Lu-Hf analyses of the G5 Supersuite from AWCO.

The field, petrographic (igneous fabric preserved and almost undeformed), lithogeochemical (alkali-calcic of I and A2 type from post-collisional tectonic environment) and geochronologic (496.5 ± 3.6 Ma from monzogabbro and 480. 9 ± 3.2 from quartz monzonite) aspects of the ACIC are similar to others G5 Supersuite plutons from AWCO. These features allowed the characterization of ACIC as one pluton of this geotectonic unit.

The ACIC is an inversely zoned pluton with about 73 km². It is make up by two monzogabbro/monzodiorite mafic cores surrounded by quartz monzonite. Between these rocks occur mingling and mixing zones, where jotunite and quartz mangerite occur. The ACIC is hosted in paragneisses of the Nova Venécia Complex and orthogneisses of the AWCO G1 Supersuite. Many host rock enclaves are enclosed in all ACIC rocks, as well as the quartz monzonite shows enclaves of monzodiorite and monzogabbro. Syenogranite and quartz-feldspar dykes cross all igneous body.

The ACIC showed itself an important pluton to better understand the post-collisional magmatism in the AWCO. Its mafic rocks showed an intense crustal contamination chemical signature, which is highlighted by the high alkalis content and relative high LREE and LILE (mainly Rb, Ba and Sr) if compared to mantle mafic igneous rocks worldwide (Sparks, 1986). The negative εHf values from monzogabbro (average value -10.41) is a determinant evidence to crustal contamination in ACIC.

The contamination in other plutons from G5 Supersuite have already been well-known (Horn and Weber-Diefenbach, 1987; Pedrosa-Soares and Wiedemann-Leonardos, 2000; Medeiros et al., 2001; Wiedemann et al., 2002; De Campos et al., 2004, 2016; Mendes et al., 2005), however the negative εHf values found in ACIC rocks are an important data to better understand this geological unit. Almost all G5 plutons have similar features and must also show negative εHf values. It is a new evidence of crustal contamination in the AWCO.

The felsic rocks from ACIC showed an apparently cogenetic geochemical signature with the ACIC mafic rocks. This is a strong evidence of a relationship among the ACIC rocks or contamination process. The quartz monzonite showed a negative εHf values similar (average value -11.78) to the monzogabbro and the T_{DM} between the quartz monzonite and monzogabbro are also similar (average values 1.72 to monzogabbro and 1.79 to quartz monzonite).

With the compilation of all data, two models can be proposed to explain the evolution of the ACIC in collapse stage of the AWCO, both models are based in crustal contamination/assimilation and fractional crystallization (AFC process). The deep faults were an important mechanism to crustal and lithospheric mantle melting and emplacement of this pluton.

The jotunite and quartz mangerite are restricted to mingling and mixing zones. These rocks were interpreted as mixing rocks between the mafic and felsic magmas in both models.

One argues in favor to intense interaction between a monzogabroic/monzodioritic magma from mantle and felsic magmas from crust in a magmatic chamber. The mafic magma assimilated many crustal material (felsic magma and host rock) and became alkali-calcic. This magma crystallized following the AFC process and formed the monzogabbro and monzodiorite. With the AWCO collapse stage continuity, the recently crystallized mafic rocks melted and produced a monzonitic magma. More host rocks also melted in this stage. This recent magma, assimilated more crustal material and became more alkali-calcic and richer in LILE and LREE and its crystallization formed the quartz monzonite. In this stage, there were two coeval magmas in the magmatic chamber (monzogabbroic/monzodioritic and monzonitic magmas). These magmas mingled and mixed and formed the jotunite, mangerite and mingling zones.

The other model is based in one model widely used to explain the G5 Supersuite. It argues in favor of interaction between two different magmas, the monzogabbroic/monzodioritic magma from lithospheric mantle and monzonitic magma from crust (Wiedemann et al., 2002; De Campos et al., 2004, 2016). The different magmas interacted in a magmatic chamber and contaminated itself and were contaminated by more crustal material. The magmas became alkali-calcic and began the differentiation process by AFC. The mafic magma formed first the monzograbbro and evolved to monzodiorite, while the felsic magma formed the quartz monzonite. In the interaction zones between these magmas, the jotunite, mangerite (mixing rocks) and mingling zones were formed.

These models that were proposed to ACIC evolution can be utilized to explain other similar plutons from AWCO G5 Supersuite.

To better understand the ACIC, there are other investigations to be done. The host rocks (including the enclaves in ACIC) need to be better studied. Lithogeochemical and geothermobarometry studies can improve the understanding about these rocks and contamination processes underwent by ACIC rocks. In addition, mineral chemistry studies in

the ACIC rocks can support to better understand the emplacement and cooling conditions of this pluton.

The mingling and mixing zones in ACIC also need to be studied in detail to better understand the relationship between the mafic and felsic rocks. The later syenogranite dykes were not studied and remain an incognita. Studies are necessary to better understand this rock and determine if there is relationship between syenogranite and ACIC rocks.

4. REFERENCES

Achterbergh, V., Ryan, C.G., Jackson, S.E., Griffin, W., 2001. Data reduction software for LA-ICP-MS, in: Sylvester, P. (Ed.), Laser-Ablation-ICPMs in the Earth Sciences: Principles and Applications. Volume 29, Mineralogical Association of Canada, Short Course Series. Mineralogical Association of Canada, Michigan, 239–243.

Alkmim, F.F., Marshak, S., Pedrosa-Soares, A.C., Peres, G.G., Cruz, S.C.P., Whittington, A., 2006. Kinematic evolution of the Araçuaí-West Congo orogen in Brazil and Africa: Nutcracker tectonics during the Neoproterozoic assembly of Gondwana. Precambrian Research 149, 43–64. https://doi.org/10.1016/j.precamres.2006.06.007

Barbarin, B., Didier, J., 1992. Genesis and evolution of mafic microgranular enclaves through various types of interaction between coexisting felsic and mafic magmas. Transactions of the Royal Society of Edinburgh: Earth Sciences 83, 145–153. https://doi.org/10.1017/S0263593300007835

Bayer, P., Schmidt-Thomé, R., Weber-Diefenbach, K., Horn, H.A., 1987. Complex concentric granitoid intrusions in the coastal mobile belt, Espírito Santo, Brazil: The Santa Angélica Pluton - an example. Geologische Rundschau 76, 357–371. https://doi.org/10.1007/BF01821080

Belém, J., 2014. Geoquímica, Geocronologia e Contexto Geotectônico do Magmatismo Máfico Associado ao Feixe de Fraturas Colatina, Estado do Espírito Santo. Ph.D. Thesis, Universidade Federal de Minas Gerais.

Boynton, W.V., 1984. Cosmochemistry of the rare earth elements; meteorite studies. In:Henderson, P. (Ed.), Rare earth element geochemistry, v.1, 63-114. Elsevier, Amsterdam.

Brito Neves, B., Cordani, U., 1991. Tectonic evolution of South America during the late Proterozoic. Precambrian Research 53, 23–40. https://doi.org/10.1016/0301-9268(91)90004-T

Chauvel, C., Lewin, E., Carpentier, M., Arndt, N.T., Marini, J.C., 2008. Role of recycled oceanic basalt and sediment in generating the Hf-Nd mantle array. Nature Geoscience 1, 64–67. https://doi.org/10.1038/ngeo.2007.51

Chen, M., Sun, M., Buslov, M.M., Cai, K., Zhao, G., Kulikova, A. V., Rubanova, E.S., 2016. Crustal melting and magma mixing in a continental arc setting: Evidence from the Yaloman intrusive complex in the Gorny Altai terrane, Central Asian Orogenic Belt.

Lithos 252–253, 76–91. https://doi.org/10.1016/j.lithos.2016.02.016

Chen, Q., Sun, M., Zhao, G., Yang, F., Long, X., Li, J., Wang, J., Yu, Y., 2017. Origin of the mafic microgranular enclaves (MMEs) and their host granitoids from the Tagong pluton in Songpan–Ganze terrane: An igneous response to the closure of the Paleo-Tethys ocean. Lithos 290–291, 1–17. https://doi.org/10.1016/j.lithos.2017.07.019

De Campos, C.P., Cezar Mendes, J., Ludka, I.P., de Medeiros, S.R., de Moura, J.C., Wallfass, C.M., 2004. A review of the Brasiliano magmatism in southern Espírito Santo, Brazil, with emphasis on post-collisional magmatism. Journal of the Virtual Explorer 17, 1–39. https://doi.org/10.3809/jvirtex.2004.00106

De Campos, C.P., de Medeiros, S.R., Mendes, J.C., Pedrosa-Soares, A.C., Dussin, I., Ludka, I.P., Dantas, E.L., 2016. Cambro-Ordovician magmatism in the Araçuaí Belt (SE Brazil): Snapshots from a post-collisional event. Journal of South American Earth Sciences 68, 248–268. https://doi.org/10.1016/j.jsames.2015.11.016

Ersoy, E.Y., 2013. PETROMODELER (Petrological Modeler): A Microsoft® Excel© spreadsheet program for modelling melting, mixing, crystallization and assimilation processes in magmatic systems. Turkish Journal of Earth Sciences 22, 115–125. https://doi.org/10.3906/yer-1104-6

Ersoy, Y., Helvaci, C., 2010. FC-AFC-FCA and mixing modeler: A Microsoft®Excel©spreadsheet program for modeling geochemical differentiation of magma by crystal fractionation, crustal assimilation and mixing. Computers and Geosciences 36, 383–390. https://doi.org/10.1016/j.cageo.2009.06.007

Féboli, W.L., Ribeiro, J.H., Heineck, C.A., Raposo, F.O., Souza, E.C., 1993. Domingos Martins, folha SF.24-V-A-III: estado do Espírito Santo. Escala:1:100.000., in: Féboli, W.L. (Ed.), Domingos Martins, Folha SF.24-V-A-III: Estado Do Espírito Santo. Escala:1:100.000. DNPM/CPRM, Brasília, 81–81.

Filho, L.M., Ribeiro, M.W., Gonzalez, S.R., Schenini, C.A., Neto, A. dos S., Palmeira, R.C. de B., Pires, J. de L., Teixeira, W., Castro, H.E.F. de, 1983. Folhas SF. 23/24. Rio de Janeiro/Vitória. Geologia, geomorfologia, pedologia, vegetação e uso potencial da terra/ Projeto RADAM Brasil, in: RADAMBRASIL (Ed.), Folhas SF. 23/24. Rio de Janeiro/Vitória. Geologia, Geomorfologia, Pedologia, Vegetação e Uso Potencial Da Terra/ Projeto RADAM Brasil. IBGE, Rio de Janeiro, 181–181.

Fourcade, S., Allegre, C.J., 1981. Trace elements behavior in granite genesis: A case study The calc-alkaline plutonic association from the Querigut complex (Pyrénées, France).

Contributions to Mineralogy and Petrology 76, 177–195. https://doi.org/10.1007/BF00371958

Fourny, A., Weis, D., Scoates, J.S., 2019. Isotopic and Trace Element Geochemistry of the Kiglapait Intrusion, Labrador: Deciphering the Mantle Source, Crustal Contributions and Processes Preserved in Mafic Layered Intrusions. Journal of Petrology 60, 553–590. https://doi.org/10.1093/petrology/egz006

Frost, B.R., Barnes, C.G., Collins, W.J., Arculus, R.J., Ellis, D.J., Frost, C.D., 2001. A Geochemical Classification for Granitic Rocks. Journal of Petrology 42, 2033–2048. https://doi.org/10.1093/petrology/42.11.2033

Gradim, C., Roncato, J., Pedrosa-Soares, A.C., Cordani, U., Dussin, I., Alkmim, F.F., Queiroga, G., Jacobsohn, T., Silva, L.C. da, Babinski, M., 2014. The hot back-arc zone of the Araçuaí orogen, Eastern Brazil: from sedimentation to granite generation. Brazilian Journal of Geology 44, 155–180. https://doi.org/10.5327/Z2317-4889201400010012

Harker, A., 1956. Petrology for students. An introduction to the study of rocks under the microscope (8a ed). Cambridge University Press, Cambridge.

Hibbard, M.J., 1995. Petrography to Petrogenesis. Ed. New Jersey, Prentice Hall.

Horn, H.A., Weber-Diefenbach, W., 1987. Geochemical and genetic studies of three invers zoned intrusive bodies of both alkaline and calc-alkaline composition in the Ribeira Mobile Belt (Espírito Santo, Brazil). Revista Brasileira de Geociências 17, 488–497.

Irvine, T.N., Baragar, W.R.A., 1971. A Guide to the Chemical Classification of the Common Volcanic Rocks. Canadian Journal of Earth Sciences 8, 523–548. https://doi.org/10.1139/e71-055

Janousek, V., Bowes, D.R., Colin, J.R., Braithwaite, Rogers, G., 2000. Microstructural and minaralogical evidence for limited involvement of magma mixing in the petrogenesis of a Hercynian high-K calc-alkaline intrusion: the Kozarovice granodiorite, Central Bohemian Pluton, Czech Republic. Transactions of the Royal Society of Edinburgh: Earth Sciences 91, 15–26. https://doi.org/10.1130/0-8137-2350-7.15

Janoušek, V., Farrow, C.M., Erban, V., 2006. Interpretation of whole-rock geochemical data in igneous geochemistry: Introducing Geochemical Data Toolkit (GCDkit). Journal of Petrology 47, 1255–1259. https://doi.org/10.1093/petrology/egl013

Kinny, P.D., Maas, R., 2003. Lu – Hf and Sm – Nd isotope systems in zircon. Reviews in Mineralogy & Geochemistry 53, 327–341. https://doi.org/10.2113/0530327

Le Bas, M.J., Le Maitre, R.W., Streckeisen, A., Zanettin, B., 1986. A chemical classification

of volcanic rocks based on the total alkali silica diagram. Journal of Petrology 27, 745–750. https://doi.org/10.1093/petrology/27.3.745

Le Maitre, R.W., Streckeisen, A., Zanettin, B., Le Bas, M.J., Bonin, B., Bateman, P., Bellieni, G., Dudek, A., Efremova, S., Keller, J., Lameyre, J., Sabine, P.A., Schmid, R., SØrensen, H., Woolley, A.R., 2002. Igneous Rock: A classification and glossary terms. Cambridge University Press, New York. https://doi.org/10.1017/CBO9780511535581

Liu, L., Qiu, J.S., Li, Z., 2013. Origin of mafic microgranular enclaves (MMEs) and their host quartz monzonites from the Muchen pluton in Zhejiang Province, Southeast China: Implications for magma mixing and crust-mantle interaction. Lithos 160–161, 145–163. https://doi.org/10.1016/j.lithos.2012.12.005

Lu, L., Zhang, K.-J., Jin, X., Zeng, L., Yan, L.-L., Santosh, M., 2019. Crustal Thickening of the Central Tibetan Plateau prior to India–Asia Collision: Evidence from Petrology, Geochronology, Geochemistry and Sr–Nd–Hf Isotopes of a K-rich Charnockite–Granite Suite in Eastern Qiangtang. Journal of Petrology 60, 827–854. https://doi.org/10.1093/petrology/egz017

Ludka, I.P., Wiedemann-Leonardos, C.M., 2000. Further Signs of an Enriched Mantle Source Under the Neoproterozoic Araçuaí-Ribeira Mobile Belt. Revista Brasileira de Geociências 30, 95–98.

Ludka, I.P., Wiedemann, C.M., Töpfner, C., 1998. On the origin of incompatible element enrichment in the Venda Nova pluton, State of Espirito Santo, southeast Brazil. Journal of South American Earth Sciences 11, 473–486. https://doi.org/doi.org/10.1016/S0895-9811(98)00028-5

Ludwig, K.R., 2003. User's Manual for Isoplot 3.75, a geochronological toolkit for Microsoft Excel, Berkeley Geochronology Center Special Publication.

Martins, V.T. d. S., Teixeira, W., Noce, C.M., Pedrosa-Soares, A.C., 2004. Sr and Nd characteristics of Brasiliano/Pan-African granitoid plutons of the Araçuaí Orogen, Southeastern Brazil: Tectonic implications. Gondwana Research 7, 75–89. https://doi.org/10.1016/S1342-937X(05)70307-5

Matteini, M., Dantas, E.L., Pimentel, M.M., Bühn, B., 2010. Combined U-Pb and Lu-Hf isotope analyses by laser ablation MC-ICP-MS: Methodology and applications. Anais da Academia Brasileira de Ciências 82, 479–491. https://doi.org/10.1590/S0001-37652010000200023

McDonough, W.F., Sun, S.S., 1995. The composition of the Earth. Chemical Geology 120,

223–253. https://doi.org/10.1016/0009-2541(94)00140-4

Medeiros, S.R., Wiedeman-Leonardos, C.M., Mendes, J.C., 2000. Post-collisional multistage magmatism in the Ribeira mobile belt; geochemical and isotopic study of the Varzea Alegre Intrusive Complex, Espírito Santo, Brazil. Revista Brasileira de Geociencias 30, 30–34. https://doi.org/10.25249/0375-7536.2000301030034

Medeiros, S.R., Wiedemann-Leonardos, C.M., Vriend, S., 2001. Evidence of mingling between contrasting magmas in a deep plutonic environment: The example of Várzea Alegre, in the Ribeira Mobile Belt, Espírito Santo, Brazil. Anais da Academia Brasileira de Ciencias 73, 99–119. https://doi.org/10.1590/S0001-37652001000100009

Mendes, J.C., De Campos, C.M.P., 2012. Norite and charnockites from the Venda Nova Pluton, SE Brazil: Intensive parameters and some petrogenetic constraints. Geoscience Frontiers 3, 789–800. https://doi.org/10.1016/j.gsf.2012.05.009

Mendes, J.C., de Medeiros, S.R., McReath, I., de Campos, C.M.P., 2005. Cambro-Ordovician magmatism in SE Brazil: U-Pb and Rb-Sr ages, combined with Sr and Nd isotopic data of Charnockitic rocks from the Varzea Alegre Complex. Gondwana Research 8, 337–345. https://doi.org/10.1016/S1342-937X(05)71139-4

Middlemost, E.A.K., 1994. Naming Materials in the Magma/Igneous Rock System. Earth-Science Reviews 37, 215–224. https://doi.org/10.1016/0012-8252(94)90029-9

Paradella, W.R., Liu, C.C., Meneses, P.R., 1978. Caracterização de maciços ácidos e diferenciados do sul do Espírito Santo através de técnicas de realces automáticos de dados do Landsat, in: I Simpósio Brasileiro de Sensoriamento Remoto. INPE, São José dos Campos, 582–596.

Pearce, J.A., Harris, N.B.W., Tindle, A.G., 1984. Trace-Element Discrimination Diagrams for the Tectonic Interpretation of Granitic-Rocks. Journal of Petrology 25, 956–983. https://doi.org/10.1093/petrology/25.4.956

Peccerillo, A., Taylor, S.R., 1976. Geochemistry of eocene calc-alkaline volcanic rocks from the Kastamonu area, Northern Turkey. Contributions to Mineralogy and Petrology 58, 63–81. https://doi.org/10.1007/BF00384745

Pedrosa-Soares, A.C., Alkmim, F.F., Tack, L., Noce, C.M., Babinski, M., Silva, L.C., Martins-Neto, M.A., 2008. Similarities and differences between the Brazilian and African counterparts of the Neoproterozoic Araçuaí-West Congo orogen. Geological Society, London, Special Publications 294, 153–172. https://doi.org/10.1144/SP294.9

Pedrosa-Soares, A.C., Campos, C.P. DE, Noce, C., Silva, L.C., Novo, T., Roncato, J., Medeiros,

S., Castañeda, C., Queiroga, G., Dantas, E., Dussin, I., Alkmim, F.F., 2011. Late Neoproterozoic – Cambrian granitic magmatism in the Araçuaí orogen (Brazil), the Eastern Brazilian Pegmatite Province and related mineral resources. Geological Society, London, Special Publications 350, 25–51. https://doi.org/10.1144/SP350.3

Pedrosa-Soares, A.C., Noce, C.M., Wiedemann, C.M., Pinto, C.P., 2001. The Araçuaí-West-Congo Orogen in Brazil: An overview of a confined orogen formed during Gondwanaland assembly. Precambrian Research 110, 307–323. https://doi.org/10.1016/S0301-9268(01)00174-7

Pedrosa-Soares, A.C., Wiedemann-Leonardos, C.M., 2000. Evolution of Araçuaí Belt and its connection to the Ribeira Belt, eastern Brazil, in: Cordani, U.G., Milani, E.J., Filho, A.T., Campos, D. de A. (Eds.), Tectonic Evolution of South America. Sociedade Brasileira de Geologia, Rio de Janeiro, 265–285. https://doi.org/10.13140/2.1.3802.5928

Peixoto, E., Pedrosa-Soares, A.C., Alkmim, F.F., Dussin, I.A., 2015. A suture-related accretionary wedge formed in the Neoproterozoic Araçuaí orogen (SE Brazil) during Western Gondwanaland assembly. Gondwana Research 27, 878–896. https://doi.org/10.1016/j.gr.2013.11.010

Quek, L.X., Ghani, A.A., Chung, S.L., Li, S., Lai, Y.M., Saidin, M., Amir Hassan, M.H., Muhammad Ali, M.A., Badruldin, M.H., Abu Bakar, A.F., 2017. Mafic microgranular enclaves (MMEs) in amphibole-bearing granites of the Bintang batholith, Main Range granite province: Evidence for a meta-igneous basement in Western Peninsular Malaysia. Journal of Asian Earth Sciences 143, 11–29. https://doi.org/10.1016/j.jseaes.2017.03.029

Ratajeski, K., Glazner, A.F., Miller, B. V, 2001. Geology and geochemistry of mafic to felsic plutonic rocks in the Cretaceous intrusive suite of Yosemite Valley , California. Geological Society of America Bulletin 113, 1486–1502. https://doi.org/10.1130/0016-7606(2001)113<1486:GAGOMT>2.0.CO;2

Richter, F., Lana, C., Stevens, G., Buick, I., Pedrosa-Soares, A.C., Alkmim, F.F., Cutts, K., 2016. Sedimentation, metamorphism and granite generation in a back-arc region: Records from the Ediacaran Nova Venécia Complex (Araçuaí Orogen, Southeastern Brazil). Precambrian Research 272, 78–100. https://doi.org/10.1016/j.precamres.2015.10.012

Sami, M., Ntaflos, T., Farahat, E.S., Mohamed, H.A., Hauzenberger, C., Ahmed, A.F., 2018. Petrogenesis and geodynamic implications of Ediacaran highly fractionated A-type granitoids in the north Arabian-Nubian Shield (Egypt): Constraints from whole-rock geochemistry and Sr-Nd isotopes. Lithos 304–307, 329–346.

https://doi.org/10.1016/j.lithos.2018.02.015

Serrano, P., Pedrosa-Soares, A., Medeiros-Júnior, E., Fonte-Boa, T., Araujo, C., Dussin, I., Queiroga, G., Lana, C., 2018. A-type Medina batholith and post-collisional anatexis in the Araçuaí orogen (SE Brazil). Lithos 320–321, 515–536. https://doi.org/10.1016/j.lithos.2018.09.009

Shand, S.J., 1943. Eruptive rocks. Their genesis, composition, classifications, and their relation to ore deposits with a chapter on meteorite (2a Ed). John Wiley & Sons, New York.

Signorelli, N., Drumind, J.B.V., Raposo, F.O., Souza, E.C., Heineck, C.A., 1993. Afonso Cláudio, folha SF.24-V-A-II: estados do Espírito Santo e Minas Gerais. Escala: 1:100.000., in: Signorelli, N. (Ed.), Afonso Cláudio, Folha SF.24-V-A-II: Estados Do Espírito Santo e Minas Gerais. Escala: 1:100.000. DNPM/CPRM, Brasília, 86–86.

Silva, J.N. da, Ferrari, P.G., 1976. Projeto Espírito Santo: relatório final. CPRM, Belo Horizonte.

Sparks, R.S.J., 1986. The role of crustal contamination in magma evolution through geological time. Earth and Planetary Science Letters 78, 211–223. https://doi.org/10.1016/0012-821X(86)90062-2

Sparks, R.S.J., Marshall, L.A., 1986. Thermal and mechanical constraints on mixing between mafic and silicic magmas. Journal of Volcanology and Geothermal Research 29, 99–124. https://doi.org/10.1016/0377-0273(86)90041-7

Streckeisen, A., 1976. To each plutonic rock its proper name. Earth Science Reviews 12, 1–33. https://doi.org/10.1016/0012-8252(76)90052-0

Streckeisen, A., 1974. How should charnockitic rocks be named? Centenaire de la Société Géologique de Belgique Géologie des Domaines Cristallins 97, 349–360. https://doi.org/10.1017/S001675680003822X

Taylor, S.R., McLennan, S.M., 1995. The geochemical evolution of the continental crust. Reviews of Geophysics 33, 241–265. https://doi.org/10.1029/95RG00262

Tedeschi, M., Novo, T., Pedrosa-Soares, A., Dussin, I., Tassinari, C., Silva, L.C., Gonçalves, L., Alkmim, F., Lana, C., Figueiredo, C., Dantas, E., Medeiros, S., De Campos, C., Corrales, F., Heilbron, M., 2016. The Ediacaran Rio Doce magmatic arc revisited (Araçuaí-Ribeira orogenic system, SE Brazil). Journal of South American Earth Sciences 68, 167–186. https://doi.org/10.1016/j.jsames.2015.11.011

Trompette, R.,1994. Geology of Western Gondwana (2000-500 Ma). Pan-African- Brasiliano aggregation of South American and Africa. CRC press, Rotterdan.

Valeriano, C. de M., Tupinambá, M., Simonetti, A., Heilbron, M., Almeida, J.C.H., Eirado, L.G., 2011. U-Pb LA-MC-ICPMS geochronology of Cambro-Ordovician post-collisional granites of the Ribeira belt, southeast Brazil: Terminal Brasiliano magmatism in central Gondwana supercontinent. Journal of South American Earth Sciences 32, 416–428. https://doi.org/10.1016/j.jsames.2011.03.003

Vervoort, J.D., 2015. Lu-Hf Dating: The Lu-Hf Isotope System, in: Jack Rink, W., W, T.J. (Eds.), Encyclopedia of Scientific Dating Methods. Springer Netherlands, 1–20. https://doi.org/10.1007/978-94-007-6326-5

Vieira, V.S., 2015. Geologia e Recursos Minerais do Estado do Espírito Santo: texto explicativo do mapa geológico e de recursos minerais, in: Vieira, V.S., Menezes, R.G. (Eds.), Geologia e Recursos Minerais Do Estado Do Espírito Santo: Texto Explicativo Do Mapa Geológico e de Recursos Minerais. CPRM, Belo Horizonte, 105–105.

Vieira, V.S., Souza, Em.C., Raposo, F.O., Sical, L.C., Heineck, C.A., 1993. Baixo Guandu, folha SE.24-Y-C-V, estados do Espírito Santo e Minas Gerais. Escala: 1:100.000., in: Vieira, V.S. (Ed.), Baixo Guandu, Folha SE.24-Y-C-V, Estados Do Espírito Santo e Minas Gerais. Escala: 1:100.000. DNPM/CPRM, Brasília, 107–107.

Whalen, J.B., Currie, K.L., Chappell, B.W., 1987. A-type granites: geochemical characteristics, discrimination and petrogenesis. Contributions to Mineralogy and Petrology 95, 407–419. https://doi.org/10.1007/BF00402202

Wiedemann, C.M., De Medeiros, S.R., Ludka, I.P., Mendes, J.C., Costa-de-Moura, J., 2002. Architecture of Late Orogenic Plutons in the Araçuaí-Ribeira Fold Belt, Southeast Brazil. Gondwana Research 5, 381–399. https://doi.org/10.1016/S1342-937X(05)70730-9

Zanon, M.L., Chaves, A. de O., Rangel, C.V.G.T., Gaburo, L., Pires, C.R., 2015. Os aspectos geológicos do Maciço Santa Angélica (ES): uma nova abordagem. Brazilian Journal of Geology 45, 609–633. https://doi.org/10.1590/2317-4889201520150005

Zhang, S.H., Zhao, Y., 2017. Cogenetic origin of mafic microgranular enclaves in calc-alkaline granitoids: The permian plutons in the northern north China block. Geosphere 13, 1–36. https://doi.org/10.1130/GES01407.1

Zhu, K.Y., Shen, Z.Y., Li, M.Y., Yu, Y.H., 2018. Interaction between mingling mafic and felsic magmas: Its roles in differentiation of a quartz monzonite and MMEs from eastern South China. Lithos 318–319, 60–77. https://doi.org/10.1016/j.lithos.2018.07.033

5. SUPPLEMENTARY MATERIAL

SUPPLEMENTARY TABLE 1: Whole-rock geochemistry analyses and normalized elements.

Sample	P 246-A	P 276-A	P 292-B	P 292-A	P 277-A	P 193-B	P 156-A	P 197-C	P 288	P 295-B
Rock	Mzg	Mzg	Mzd	Mzg	Mzd	Jot	Mzd	Qmag	Qmoz	Qmoz
Major elements										
SiO_2	49.4	50.42	51.17	51.36	52.35	53.29	54.99	55.7	59.68	62.28
TiO_2	2.6	2.97	2.71	2.97	2.34	2.43	2.53	1.67	1.18	1.55
Fe_2O_3	11.59	12.42	11.92	11.22	10.06	10.89	10.73	9.09	7.07	7.96
Al_2O_3	15.33	15.31	16.8	14.51	16.13	13.79	14.96	15.92	15.76	14.32
MgO	6.3	3.71	3.38	4.68	3.05	2.66	3.93	2.04	1.41	1.73
MnO	0.17	0.19	0.18	0.17	0.15	0.2	0.15	0.08	0.12	0.12
CaO	8.46	7.33	6.49	7.76	6.34	5.78	6.59	4.91	4.11	4.05
K_2O	1.98	2.47	3.95	2.37	3.12	3.43	2.95	3.52	3.9	3.57
Na_2O	3.16	3.21	3.85	3.14	3.4	2.9	2.94	3.76	3.43	3.45
P_2O_5	1.15	1.36	1.18	1.32	1.07	1.12	1.11	0.71	0.49	0.52
Cr_2O_3	0.02	<0.01	<0.01	<0.01	<0.01	<0.01	<0.01	<0.01	<0.01	<0.01
LOI	0.2	0.14	0.14	0.64	1.48	0.26	0.33	1.08	0.09	0.56
Sum	100.36	99.53	101.76	100.14	99.52	96.75	101.21	98.48	97.24	100.11
CIPW Norm										
Q	0	0	0	0.67	1.04	5.66	5.22	4.37	11.57	14.98
C	0	0	0	0	0	0	0	0	0	0
Or	11.68	14.68	22.97	14.07	18.81	21.00	17.28	21.35	23.72	21.19
Ab	26.70	27.33	27.89	26.70	29.35	25.42	24.65	32.66	29.87	29.32
An	21.76	20.19	16.62	18.58	19.93	15.00	18.74	16.59	16.55	13.10
Ne	0	0	2.25	0	0	0	0	0	0	0
Di(FS)	4.60	3.66	3.78	4.68	2.46	3.85	2.89	2.06	0.68	2.10
Di(MS)	5.82	2.60	2.51	4.81	1.76	2.17	2.51	1.03	0.29	1.02
Hy(MS)	3.93	7.62	0	9.48	6.93	5.85	8.53	4.73	3.47	3.85
Hy(FS)	3.56	12.32	0	10.59	11.14	11.88	11.28	10.86	9.28	9.08
Ol(MS)	6.33	0.32	4.98	0	0	0	0	0	0	0
Ol(FS)	6.32	0.58	9.51	0	0	0	0	0	0	0
Mt	1.68	1.81	1.70	1.63	1.49	1.64	1.54	1.35	1.05	1.16
Il	4.93	5.67	5.06	5.67	4.53	4.78	4.76	3.25	2.30	2.95
Ap	2.66	3.16	2.69	3.07	2.53	2.69	2.54	1.68	1.16	1.20
Trace elements										
Ni	88	36	12	50	21	10	30	11	10	12
Co	36.3	30.3	24.4	70.7	21.4	23.9	22	16.4	9.5	13.1
Rb	39.6	36.5	77.5	52.5	77.2	78.8	78	81	80.3	103.2
Ba	1980	2482	4081	2435	2960	2609	1964	2875	4492	1966
Sr	1238	818	1171	1156	1150	824	879	993	1003	627
Zr	352	556	701	595	628	489	446	1019	837	832
Nb	21.47	33.16	34.61	29.06	26.96	31.32	23.69	14.73	20.54	43.52
Y	30.76	45.24	42.86	36.55	31.52	37.94	31.74	26.23	30.48	85.34
Ta	0.6	0.88	0.92	1.02	0.81	0.91	0.64	<0.05	0.18	2.23
Hf	7.48	11.81	13.94	15.2	13.21	11.59	9.94	21.91	18.41	20.36
Th	4.2	2.2	4.7	5.7	7.8	5.4	9.9	5	9.3	17.3
U	0.77	0.33	0.8	0.92	1.48	0.6	1.32	0.99	0.76	1.29
Zn	130	174	168	148	138	149	131	139	156	142
V	229	227	191	224	160	205	235	135	80	109
Cs	0.52	0.39	0.6	0.34	1.69	0.43	1.37	0.91	0.69	0.49
Cu	33	19	20	29	21	18	17	17	16	13
Ga	18.5	21.3	24	21.5	21	21.2	20.9	25	22.8	24.4
Gd	11.53	16.93	16.05	13.98	12.24	13.72	11.66	10.51	13.01	26.73
Mo	<2	<2	<2	2	<2	<2	<2	<2	<2	<2
Sn	<0.3	<0.3	<0.3	<0.3	<0.3	<0.3	<0.3	<0.3	<0.3	<0.3
Tl	<0.5	<0.5	<0.5	<0.5	<0.5	<0.5	<0.5	<0.5	<0.5	<0.5
W	1.4	1.6	2.9	213	2.2	1.4	1.3	1.3	3	1.3
Rare-earth elements										
La	93.3	113.4	145.3	130.1	109.2	110.3	86.7	121.8	150.2	184.5
Ce	191.1	250.4	297	265	228.9	230.3	178.7	241.6	299.4	415.5
Pr	22.59	31.22	35.66	30.87	27.05	27.76	21.71	27.11	34.48	52.64
Nd	87.3	128	135.7	120.6	102.3	110.7	86.5	100.3	128.2	212.4
Sm	15.2	22.8	21.9	19.7	17.4	18.6	15.3	15.5	19.8	39
Eu	3.52	4.52	5.08	4.51	4.02	4.33	3.53	3.88	4.95	5.38
Gd	11.53	16.93	16.05	13.98	12.24	13.72	11.66	10.51	13.01	26.73
Tb	1.36	2.02	1.88	1.66	1.44	1.71	1.41	1.21	1.45	3.55
Dy	6.94	10.58	9.82	8.22	7.05	8.73	7.22	5.9	7.16	19.14
Ho	1.2	1.8	1.69	1.39	1.21	1.43	1.24	0.97	1.18	3.23
Er	3.16	4.62	4.31	3.67	3.24	3.88	3.3	2.59	3.09	8.21
Tm	0.4	0.56	0.55	0.46	0.4	0.52	0.41	0.33	0.38	0.98
Yb	2.5	3.5	3.3	3	2.5	3.1	2.5	2.1	2.3	5.8
Lu	0.36	0.5	0.48	0.42	0.35	0.44	0.36	0.31	0.34	0.77

Sample	P 285-B	P 206-D	P 98	P 297	P 296	P 146-B	P 291	P 298	P 90-A	P 102
Rock	Qmoz	Qmoz	Qmoz	Qmoz	Qmoz	Qmoz	Qmoz	Qmoz	Qmoz	Qmoz
Major elements										
SiO_2	62.37	62.81	63.65	65.27	65.43	66.65	66.71	66.77	66.86	69.08
TiO_2	1.15	0.9	1.07	0.86	1.33	0.94	1.07	0.6	0.69	1.01
Fe_2O_3	6.62	5.21	5.24	4.13	6.86	5.36	5.35	4.05	3.97	5.3
Al_2O_3	15.09	15.8	14.96	16.06	14.58	14.39	14.5	16.29	14.44	13.79
MgO	1.4	1.02	1.33	1	1.53	1.17	1.22	0.72	0.77	1.2
MnO	0.12	0.1	0.08	0.06	0.11	0.09	0.09	0.07	0.08	0.09
CaO	3.69	4.07	3.36	2.67	3.6	2.98	3.07	2.87	2.17	2.67
K_2O	4.57	4.12	5.15	6.01	4.69	5	4.98	4.62	5.69	4.87
Na_2O	3.17	3.37	3.21	3.43	3.05	3.11	3.25	3.78	3.19	3.13
P_2O_5	0.47	0.35	0.41	0.31	0.49	0.37	0.39	0.21	0.26	0.34
Cr_2O_3	<0.01	<0.01	<0.01	<0.01	<0.01	<0.01	<0.01	<0.01	<0.01	<0.01
LOI	0.14	0.32	0.87	0.21	0.59	0.51	0.14	0.32	0.22	0.36
Sum	98.8	98.07	99.35	100.01	102.26	100.58	100.77	100.31	98.34	101.84
CIPW Norm										
Q	14.38	15.86	15.06	13.77	17.36	19.52	18.75	17.96	19.61	22.64
C	0	0	0	0	0	0	0	0.35	0	0
Or	27.37	24.90	30.91	35.58	27.26	29.53	29.24	27.30	34.27	28.36
Ab	27.18	29.17	27.58	29.08	25.38	26.29	27.33	31.99	27.50	26.09
An	13.63	16.17	11.37	10.69	12.04	10.53	10.2	12.87	8.43	9.06
Ne	0	0	0	0	0	0	0	0	0	0
Di(FS)	1.05	1.28	1.52	0.29	1.35	1.05	1.34	0	0.48	1.02
Di(MS)	0.48	0.54	0.87	0.16	0.67	0.50	0.69	0	0.20	0.51
Hy(MS)	3.30	2.34	2.95	2.42	3.43	2.67	2.69	1.79	1.86	2.70
Hy(FS)	8.27	6.35	5.89	5.02	7.91	6.46	6.03	5.49	5.08	6.17
Ol(MS)	0	0	0	0	0	0	0	0	0	0
Ol(FS)	0	0	0	0	0	0	0	0	0	0
Mt	0.97	0.77	0.77	0.60	0.98	0.77	0.77	0.58	0.58	0.75
Il	2.21	1.74	2.06	1.63	2.48	1.78	2.01	1.14	1.33	1.89
Ap	1.10	0.82	0.96	0.72	1.11	0.85	0.89	0.48	0.61	0.77
Trace elements										
Ni	9	10	13	10	12	12	10	11	8	10
Co	9.9	7.2	10.5	8	12.8	7.9	9.7	5.3	5.5	8.7
Rb	89.2	82.6	134.7	144	116.7	117	131.1	113.9	138.8	130.4
Ba	4735	4307	3059	3635	2798	2999	2772	3327	2926	2545
Sr	898	935	741	809	685	705	635	764	641	586
Zr	854	806	458	413	647	555	586	529	412	533
Nb	17.32	20.59	19.78	18.69	27.98	22.54	26.75	15.9	16.75	27.32
Y	38.03	30.45	24.61	26.22	38.64	38.9	36.99	30.65	30.38	37.16
Ta	0.2	0.16	1.39	0.42	0.64	1.17	0.5	0.34	0.26	0.67
Hf	18.13	18.97	11.95	8.29	14.62	13.41	12.67	11.64	9.96	13.14
Th	6.6	7.5	16.4	9	10.4	15.7	12.9	19.8	16.9	14.6
U	0.6	0.62	2.11	1.92	1.02	1.1	1.2	1.26	1.86	1.45
Zn	115	102	82	68	106	104	98	84	79	98
V	75	61	83	78	98	60	63	45	50	72
Cs	0.44	0.42	2.2	2.22	0.69	0.59	1.14	1.88	1.25	1.13
Cu	8	8	9	7	18	5	16	6	11	11
Ga	22.4	24.1	21.7	23.1	22.2	21.8	22.8	20.8	20.5	21.5
Gd	13.53	12.69	9.41	7.92	13.74	14.16	12.71	13.43	12.87	12.89
Mo	<2	<2	<2	<2	<2	<2	<2	<2	<2	<2
Sn	<0.3	<0.3	<0.3	<0.3	<0.3	<0.3	<0.3	<0.3	<0.3	1.5
Tl	<0.5	<0.5	1	<0.5	<0.5	0.7	<0.5	<0.5	<0.5	<0.5
W	1.2	1.7	1.8	1.5	0.8	1.1	1.7	1.6	1.4	1.6
Rare-earth elements										
La	129.7	132.1	113.7	79.8	128.8	152.9	135.2	221.4	302.6	141.5
Ce	267.7	264.1	225.2	157.2	262.5	316	274.6	457	303.2	281.2
Pr	31.54	30.59	25	18.71	30.96	36.4	30.95	46.61	50.32	31.62
Nd	122.1	116.6	88.8	66.7	116.4	130.4	113.2	159.9	166	113.8
Sm	19.5	18.5	13.6	11.2	18.7	20.5	19.1	22	20.6	18.7
Eu	4.73	5.16	2.91	2.74	3.65	3.81	3.5	4.31	4.73	3.38
Gd	13.53	12.69	9.41	7.92	13.74	14.16	12.71	13.43	12.87	12.89
Tb	1.58	1.47	1.09	0.99	1.63	1.64	1.57	1.51	1.38	1.57
Dy	7.98	7.2	5.48	5.11	8.51	8.48	8.15	7.42	6.22	7.87
Ho	1.38	1.21	0.97	0.92	1.37	1.47	1.36	1.24	1.06	1.37
Er	3.81	3.31	2.46	2.45	3.67	3.64	3.52	3.16	2.58	3.69
Tm	0.44	0.4	0.34	0.33	0.49	0.48	0.47	0.41	0.35	0.47
Yb	2.7	2.5	2.1	2.1	2.9	3.1	2.9	2.5	2.2	3
Lu	0.39	0.35	0.34	0.31	0.41	0.44	0.4	0.38	0.33	0.4

Chondrite Normalized elements (Boyton, 1984)										
Sample	**P 246-A**	**P 276-A**	**P 292-B**	**P 292-A**	**P 277-A**	**P 193-B**	**P 156-A**	**P 197-C**	**P 288**	**P 295-B**
Rock	**Mzg**	**Mzg**	**Mzd**	**Mzg**	**Mzd**	**Jot**	**Mzd**	**Qmag**	**Qmoz**	**Qmoz**
La_N	300.97	365.81	468.71	419.68	352.26	355.81	279.68	392.9	484.52	595.16
Ce_N	236.51	309.9	367.57	327.97	283.29	285.02	221.16	299.01	370.54	514.23
Pr_N	185.16	255.9	292.3	253.03	221.72	227.54	177.95	222.21	282.62	431.48
Nd_N	145.5	213.33	226.17	201	170.5	184.5	144.17	167.17	213.67	354
Sm_N	77.95	116.92	112.31	101.03	89.23	95.38	78.46	79.49	101.54	200
Eu_N	47.89	61.5	69.12	61.36	54.69	58.91	48.03	52.79	67.35	73.2
Gd_N	44.52	65.37	61.97	53.98	47.26	52.97	45.02	40.58	50.23	103.2
Tb_N	28.69	42.62	39.66	35.02	30.38	36.08	29.75	25.53	30.59	74.89
Dy_N	21.55	32.86	30.5	25.53	21.89	27.11	22.42	18.32	22.24	59.44
Ho_N	16.71	25.07	23.54	19.36	16.85	19.92	17.27	13.51	16.43	44.99
Er_N	15.05	22	20.52	17.48	15.43	18.48	15.71	12.33	14.71	39.1
Tm_N	12.35	17.28	16.98	14.2	12.35	16.05	12.65	10.19	11.73	30.25
Yb_N	11.96	16.75	15.79	14.35	11.96	14.83	11.96	10.05	11	27.75
Lu_N	11.18	15.53	14.91	13.04	10.87	13.66	11.18	9.63	10.56	23.91
Eu/Eu*	0.81	0.7	0.83	0.83	0.84	0.83	0.81	0.93	0.94	0.51
La_N/Yb_N	25.16	21.84	29.68	29.24	29.45	23.99	23.38	39.1	44.03	21.45
La_N/Sm_N	3.86	3.13	4.17	4.15	3.95	3.73	3.56	4.94	4.77	2.98
Ce_N/Yb_N	19.77	18.51	23.28	22.85	23.68	19.22	18.49	29.76	33.67	18.53
Ce_N/Sm_N	3.03	2.65	3.27	3.25	3.17	2.99	2.82	3.76	3.65	2.57
Eu_N/Yb_N	4	3.67	4.38	4.27	4.57	3.97	4.02	5.25	6.12	2.64
Ga_N/Yb_N	3.72	3.90	3.92	3.76	3.95	3.57	3.764	4.03	4.56	3.71
Sample	**P 285-B**	**P 206-D**	**P 296**	**P 98**	**P 297**	**P 146-B**	**P 291**	**P 298**	**P 90-A**	**P 102**
Rock	**Qmoz**	**Qmoz**	**Qmoz**	**Qmoz**	**Qmoz**	**Qmoz**	**Qmoz**	**Qmoz**	**Qmoz**	**Qmoz**
La_N	418.39	426.13	415.48	366.77	257.42	493.23	436.13	714.19	976.13	456.45
Ce_N	331.31	326.86	324.88	278.71	194.55	391.09	339.85	565.59	375.25	348.02
Pr_N	258.52	250.74	253.77	204.92	153.36	298.36	253.69	382.05	412.46	259.18
Nd_N	203.5	194.33	194	148	111.17	217.33	188.67	266.5	276.67	189.67
Sm_N	100	94.87	95.9	69.74	57.44	105.13	97.95	112.82	105.64	95.9
Eu_N	64.35	70.2	49.66	39.59	37.28	51.84	47.62	58.64	64.35	45.99
Gd_N	52.24	49	53.05	36.33	30.58	54.67	49.07	51.85	49.69	49.77
Tb_N	33.33	31.01	34.39	23	20.89	34.6	33.12	31.86	29.11	33.12
Dy_N	24.78	22.36	26.43	17.02	15.87	26.34	25.31	23.04	19.32	24.44
Ho_N	19.22	16.85	19.08	13.51	12.81	20.47	18.94	17.27	14.76	19.08
Er_N	18.14	15.76	17.48	11.71	11.67	17.33	16.76	15.05	12.29	17.57
Tm_N	13.58	12.35	15.12	10.49	10.19	14.81	14.51	12.65	10.8	14.51
Yb_N	12.92	11.96	13.88	10.05	10.05	14.83	13.88	11.96	10.53	14.35
Lu_N	12.11	10.87	12.73	10.56	9.63	13.66	12.42	11.8	10.25	12.42
Eu/Eu*	0.89	1.03	0.7	0.79	0.89	0.68	0.69	0.77	0.89	0.67
La_N/Yb_N	32.39	35.62	29.94	36.5	25.62	33.25	31.43	59.71	92.73	31.8
La_N/Sm_N	4.18	4.49	4.33	5.26	4.48	4.69	4.45	6.33	9.24	4.76
Ce_N/Yb_N	25.65	27.33	23.41	27.74	19.36	26.37	24.49	47.28	35.65	24.25
Ce_N/Sm_N	3.31	3.45	3.39	4	3.39	3.72	3.47	5.01	3.55	3.63
Eu_N/Yb_N	4.98	5.87	3.58	3.94	3.71	3.49	3.43	4.9	6.11	3.2
Ga_N/Yb_N	4.04	4.09	3.82	3.61	3.04	3.68	3.53	4.33	4.71	3.46
$Eu/Eu^* = Eu_N/[(Sm_N) + (Gd_N)]^{1/2}$										

Abreviations: Mzg= Monzogabbro; Mzd= Monzodiorite; Jot = Jotunite; Qmag= Quartz mangerite; Qmoz= Quartz monzonite.

SUPPLEMENTARY TABLE 2: ACIC Zircon U-Pb analyses and standards.

					Ratios [d]								
Analyzed spots	**^{207}Pb (cps) [a]**	**^{206}Pb (cps) [a]**	**U (ppm) [b]**	**Th/ U [c]**	**^{207}Pb/^{206}Pb**	**2σ (%)**	**^{207}Pb/^{235}U**	**2σ (%)**	**^{206}Pb/^{238}U**	**2σ (%)**	**Rho [e]**	**^{208}Pb/^{232}Th**	**2σ (%)**
Quartz monzonite													
ACIC007	426960	24441	260.62	1.65	0.06	1.41	0.60	2.17	0.08	1.65	0.76	0.02	1.25
ACIC008	489057	27999	298.93	1.67	0.06	1.19	0.60	1.98	0.08	1.57	0.80	0.02	0.94
ACIC009	400345	22828	240.44	2.57	0.06	1.10	0.61	1.88	0.08	1.53	0.81	0.02	0.94
ACIC010	395181	22790	239.43	2.01	0.06	1.08	0.61	1.88	0.08	1.54	0.82	0.02	0.95
ACIC011	559472	32291	342.81	1.89	0.06	1.04	0.61	1.83	0.08	1.51	0.82	0.02	0.86
ACIC012	635987	36959	378.07	2.17	0.06	3.59	0.63	4.57	0.08	2.83	0.62	0.02	0.83
ACIC013	588885	33992	358.05	2.00	0.06	1.16	0.61	1.93	0.08	1.54	0.80	0.02	1.11
ACIC014	533487	30916	325.69	2.45	0.06	1.05	0.61	1.85	0.08	1.53	0.82	0.02	0.95
ACIC015	389507	22418	235.87	1.93	0.06	1.69	0.61	2.48	0.08	1.81	0.73	0.02	0.90
ACIC016	347585	20184	208.32	2.27	0.06	1.14	0.62	1.92	0.08	1.55	0.81	0.02	1.03
ACIC017	380800	22095	227.87	1.42	0.06	1.00	0.62	1.84	0.08	1.54	0.84	0.02	0.88
ACIC019	560302	32293	336.79	1.41	0.06	3.62	0.62	4.63	0.08	2.88	0.62	0.02	1.04
ACIC027	237527	13636	147.31	2.13	0.06	1.13	0.60	1.98	0.08	1.63	0.82	0.02	1.12
ACIC028	740892	42920	443.03	2.24	0.06	1.02	0.62	1.85	0.08	1.54	0.83	0.02	0.88
ACIC029	416453	24021	253.15	3.04	0.06	1.07	0.61	1.90	0.08	1.57	0.82	0.02	0.97
ACIC030	780817	44981	478.50	2.29	0.06	1.03	0.61	1.85	0.08	1.53	0.83	0.02	0.90
ACIC032	335027	19098	203.58	2.06	0.06	2.49	0.60	3.31	0.08	2.19	0.66	0.02	1.43
ACIC033	146337	8381	90.74	4.26	0.06	1.22	0.59	2.01	0.08	1.60	0.79	0.02	0.98
ACIC036	300041	17232	182.32	1.92	0.06	1.19	0.61	2.01	0.08	1.61	0.80	0.02	0.99
ACIC038	363050	20872	217.78	1.88	0.06	1.04	0.62	1.89	0.08	1.57	0.83	0.02	1.01
ACIC039	635571	36424	383.85	2.63	0.06	1.19	0.61	2.00	0.08	1.62	0.81	0.02	0.90
ACIC040	289684	16668	176.67	0.73	0.06	1.04	0.61	1.89	0.08	1.57	0.83	0.02	1.20
Monzogabbro													
ACIC047	195614	11412	117.27	4.67	0.06	1.30	0.63	2.10	0.08	1.64	0.78	0.02	1.20
ACIC048	135100	7843	80.76	4.15	0.06	1.19	0.63	2.04	0.08	1.66	0.81	0.02	0.98
ACIC052	273508	15898	162.86	4.29	0.06	3.62	0.63	4.64	0.08	2.90	0.63	0.02	1.04
ACIC053	112959	6583	67.83	4.38	0.06	2.13	0.62	2.93	0.08	2.01	0.69	0.02	1.40
ACIC054	540851	31045	326.37	5.58	0.06	3.66	0.61	4.68	0.08	2.91	0.62	0.02	1.18
ACIC056	701407	40759	414.28	5.45	0.06	1.08	0.63	1.93	0.08	1.60	0.83	0.02	1.16
ACIC057	438113	25311	254.38	5.51	0.06	3.62	0.64	4.60	0.08	2.84	0.62	0.02	0.98
ACIC059	279013	16125	163.24	6.00	0.06	1.08	0.64	1.95	0.08	1.63	0.83	0.02	0.95
ACIC068	158427	9184	93.72	2.86	0.06	1.29	0.63	2.15	0.08	1.72	0.80	0.02	1.33
ACIC069	185316	10752	110.47	2.43	0.06	1.36	0.63	2.20	0.08	1.73	0.79	0.02	1.13
ACIC071	242446	14173	145.64	4.55	0.06	1.16	0.63	2.06	0.08	1.70	0.82	0.02	1.23
ACIC072	199459	11506	118.53	3.36	0.06	2.37	0.62	3.21	0.08	2.17	0.68	0.02	1.40
ACIC073	278044	16324	159.37	5.38	0.06	1.19	0.66	2.07	0.08	1.69	0.82	0.02	1.27
ACIC075	232982	13457	136.41	4.89	0.06	1.11	0.63	2.03	0.08	1.70	0.84	0.02	1.08
ACIC076	248720	14426	146.94	5.04	0.06	1.14	0.63	2.02	0.08	1.67	0.83	0.02	1.13
ACIC077	235570	13717	140.14	5.18	0.06	1.31	0.63	2.17	0.08	1.73	0.80	0.02	1.42
ACIC079	348953	20239	205.76	4.90	0.06	1.02	0.63	1.97	0.08	1.69	0.86	0.02	0.99
ACIC080	112349	6450	66.41	2.60	0.06	3.56	0.63	4.57	0.08	2.86	0.63	0.02	1.24

	Ages (Ma)								
Analyzed	**$^{207}Pb/^{206}P$**	**2σ**	**$^{206}Pb/^{238}$**	**2σ**	**$^{207}Pb/^{235}$**	**2σ**	**$^{208}Pb/^{232}T$**	**2σ**	**Concordia (%)**
Quartz monzonite									
ACIC007	478.80	31.05	479.64	8.00	479.50	8.65	477.90	6.10	100.10
ACIC008	479.06	26.30	479.02	7.62	479.02	7.87	468.70	4.54	100.07
ACIC009	470.10	24.36	487.20	7.51	484.22	7.56	468.70	4.42	100.69
ACIC010	495.14	23.60	483.11	7.51	485.21	7.54	461.40	4.32	99.65
ACIC011	496.91	22.82	477.88	7.28	481.17	7.31	463.40	4.14	99.39
ACIC012	511.97	78.56	492.03	14.08	495.57	18.77	481.10	4.12	99.38
ACIC013	497.15	25.48	481.46	7.49	484.19	7.74	469.40	4.96	99.51
ACIC014	505.80	23.07	479.59	7.40	484.15	7.44	464.80	4.20	99.13
ACIC015	490.77	37.20	483.34	8.82	484.64	9.95	444.50	3.80	99.81
ACIC016	510.35	24.89	488.17	7.63	492.08	7.80	465.70	4.92	99.30
ACIC017	508.57	21.92	488.91	7.63	492.38	7.48	452.10	3.86	99.39
ACIC019	493.82	79.56	486.80	14.16	488.04	18.78	459.10	4.56	99.83
ACIC027	485.17	24.90	472.36	7.76	474.55	7.83	430.00	4.64	99.60
ACIC028	505.04	22.32	489.25	7.62	492.04	7.51	456.70	4.14	99.52
ACIC029	495.52	23.60	481.58	7.63	484.00	7.63	454.20	4.28	99.57
ACIC030	492.77	22.68	477.82	7.41	480.41	7.38	443.40	4.12	99.53
ACIC032	469.55	54.96	481.75	10.64	479.63	13.24	448.50	6.42	100.51
ACIC033	479.78	26.91	472.41	7.64	473.67	7.95	447.70	4.44	99.79
ACIC036	485.97	26.20	481.75	7.85	482.48	8.03	444.00	4.36	99.92
ACIC038	488.25	22.94	487.77	7.74	487.85	7.61	434.40	4.22	100.07
ACIC039	481.26	26.09	484.59	7.92	484.01	8.04	445.60	4.06	100.20
ACIC040	490.16	22.91	480.04	7.64	481.80	7.55	433.90	5.30	99.71
Monzogabbro									
ACIC047	520.54	28.48	488.05	8.10	493.80	8.55	431.80	5.12	98.93
ACIC048	509.60	26.03	489.42	8.22	492.99	8.32	408.40	4.06	99.37
ACIC052	512.47	79.32	491.23	14.41	495.00	19.05	422.50	4.50	99.34
ACIC053	518.31	46.58	487.26	9.87	492.74	11.92	427.80	5.78	98.98
ACIC054	484.81	80.58	484.99	14.29	484.96	18.91	441.30	5.16	100.08
ACIC056	511.87	23.74	495.09	7.97	498.09	7.91	449.80	5.18	99.50
ACIC057	499.03	79.41	503.32	14.45	502.54	19.11	446.70	4.46	100.26
ACIC059	499.78	23.66	499.63	8.21	499.66	8.03	421.10	4.04	100.10
ACIC068	506.56	28.35	494.36	8.57	496.53	8.80	422.50	5.58	99.66
ACIC069	508.39	29.84	490.72	8.59	493.85	8.99	423.80	4.84	99.46
ACIC071	525.05	25.41	487.09	8.34	493.80	8.38	421.90	4.96	98.74
ACIC072	495.72	51.97	492.20	10.80	492.82	13.10	427.40	5.78	99.97
ACIC073	534.40	26.00	509.60	8.67	514.15	8.68	442.40	5.56	99.25
ACIC075	498.57	24.31	499.29	8.56	499.16	8.33	407.90	4.26	100.13
ACIC076	507.70	24.93	494.98	8.33	497.25	8.27	424.50	4.88	99.64
ACIC077	516.40	28.58	491.69	8.58	496.08	8.86	424.00	5.96	99.21
ACIC079	507.70	22.29	495.89	8.45	498.00	8.08	404.80	4.06	99.68
ACIC080	485.32	78.37	494.70	14.28	493.03	18.69	387.10	4.76	100.43

					Ratios[d]								
Analyzed spots	**^{207}Pb (cps) [a]**	**^{206}Pb (cps) [a]**	**U (ppm) [b]**	**Th/U [c]**	**^{207}Pb/^{206}Pb**	**2σ (%)**	**^{207}Pb/^{235}**	**2σ (%)**	**^{206}Pb/^{238}U**	**2σ (%)**	**Rho [e]**	**^{208}Pb/^{232}Th**	**2σ (%)**
PRIMARY REF. MAT. (GJ-1 zircon)													
Spot001	1110622	65779	598.80	0.46	0.059	3.52	0.75	4.39	0.09	2.62	0.59	0.028	0.9
Spot002	1135399	67613	616.98	0.44	0.059	1.00	0.74	1.79	0.09	1.48	0.82	0.028	0.9
Spot021	830372	48754	470.13	0.44	0.058	1.10	0.70	1.88	0.08	1.53	0.81	0.028	1.4
Spot022	867559	51419	481.40	0.45	0.059	1.39	0.73	2.21	0.08	1.72	0.77	0.029	1.0
Spot041	727558	41631	404.80	0.45	0.057	3.64	0.70	4.56	0.08	2.73	0.60	0.026	1.3
Spot042	758807	43418	412.57	0.46	0.057	0.99	0.71	1.86	0.09	1.57	0.84	0.027	1.1
Spot061	595590	37730	317.29	0.42	0.063	1.08	0.81	2.01	0.09	1.69	0.84	0.034	1.5
Spot081	745006	46422	400.19	0.49	0.062	1.42	0.79	2.27	0.09	1.78	0.78	0.027	2.4
Spot082	803267	47652	432.76	0.50	0.059	1.06	0.75	1.99	0.09	1.69	0.84	0.028	1.2
SECONDARY REF. MAT. (Plešovice and Blue Berry													
Spot003	1376738	73751	1202.4	0.25	0.053	0.98	0.39	1.77	0.05	1.47	0.83	0.017	1.0
Spot023	1133107	60744	999.13	0.31	0.053	1.04	0.39	1.91	0.05	1.60	0.83	0.018	1.0
Spot043	1076156	57767	954.17	0.34	0.053	0.98	0.38	1.85	0.05	1.57	0.84	0.016	1.1
Spot044	925414	48830	818.90	0.30	0.052	3.94	0.38	5.56	0.05	3.92	0.70	0.016	1.6
Spot064	747433	39808	653.13	0.27	0.052	1.05	0.39	1.93	0.05	1.62	0.83	0.015	1.6
Spot083	807706	43052	691.55	0.27	0.052	3.88	0.40	5.45	0.05	3.82	0.70	0.015	1.4
Spot084	882870	47348	758.66	0.27	0.053	0.96	0.40	1.92	0.05	1.66	0.86	0.017	1.2
Spot005	124810	67258	1100.5	0.25	0.053	1.00	0.39	1.81	0.05	1.43	0.83	0.017	1.0
Spot006	106187	57510	934.16	0.23	0.053	1.03	0.39	1.82	0.05	1.42	0.82	0.018	1.1
Spot025	864849	46624	771.78	0.26	0.053	0.96	0.38	1.82	0.05	1.47	0.84	0.019	1.0
Spot065	633908	33839	549.86	0.25	0.052	1.10	0.39	1.97	0.05	1.55	0.83	0.018	1.6

	Ages (Ma)								
Analyzed spots	**^{207}Pb/^{206}Pb**	**2σ (abs)**	**^{206}Pb/^{238}U**	**2σ (abs)**	**^{207}Pb/^{235}U**	**2σ (abs)**	**^{208}Pb/^{232}Th**	**2σ (abs)**	**Concordia (%) [f]**
PRIMARY REF. MAT. (GJ-1 zircon)									
Spot001	575.48	76.64	567.4	14.2	569.02	19.33	563.7	5.48	99.71
Spot002	587.26	21.86	563.1	8.03	567.96	7.85	576.4	5.68	99.15
Spot021	556.50	24.00	541.4	7.96	544.34	7.98	557.5	7.9	99.46
Spot022	577.00	30.29	551.9	9.14	556.89	9.55	589.3	6.1	99.11
Spot041	500.03	80.35	550.5	14.4	540.83	19.31	527.9	7.04	101.79
Spot042	500.02	21.93	562.8	8.51	550.57	7.96	541	5.96	102.23
Spot061	720.00	23.11	573.9	9.32	604.34	9.22	674.7	10.7	94.97
Spot081	684.83	30.35	569.4	9.71	593.11	10.28	542.9	12.98	96.00
Spot082	578.97	23.13	567.8	9.19	570.05	8.75	566	6.96	99.60
SECONDARY REF. MAT. (Plešovice and Blue Berry zircons)									
Spot003	330.26	22.35	338.9	5.12	337.84	5.35	357	3.54	100.11
Spot023	331.92	23.71	335.8	5.49	335.31	5.72	365.9	3.84	99.93
Spot043	334.90	22.28	333.9	5.37	334.11	5.53	320	3.76	99.75
Spot044	295.86	89.58	334.6	13.4	329.80	16.49	320.2	5.34	101.23
Spot064	317.08	23.80	338.7	5.61	336.02	5.78	319.2	5.1	100.60
Spot083	318.88	87.87	345.5	13.5	342.13	16.67	314.3	4.42	100.80
Spot084	332.80	21.89	344.3	5.85	342.86	5.86	343.5	4.26	100.23
Spot005	343.70	22.69	335.8	5.17	336.80	5.43	344.7	3.56	99.49
Spot006	355.05	23.30	336.5	5.17	338.90	5.50	369.6	4.4	99.10
Spot025	344.59	21.73	331.9	5.25	333.49	5.42	380.6	3.84	99.30
Spot065	322.28	24.91	341.2	5.71	338.79	5.95	377	6.16	100.50

a= Within-run background-corrected mean signal; ^{206}Pb and ^{207}Pb are in counts per second (cps);

b= Concentration uncertainty ca. 20%;

c= U and Pb content and Th/U ratio were calculated relative to GJ-1 reference zircon;

d= Corrected for common Pb using Stacy and Kramers (1975) model Pb composition;

e= Rho is the error correlation defined as the quotient of the propagated errors of the ^{206}Pb/^{238}U and the ^{207}Pb/^{235}U ratio;

f= Degree of concordance=(^{238}U/^{206}Pb age×100/^{207}Pb/^{206}Pb age);

SUPPLEMENTARY TABLE 3: ACIC Zircon Lu-Hf analyses and standards.

Spot	$^{176}Yb/^{177}Hf$ [a]	±2σ	$^{176}Lu/^{177}Hf$ [a]	±2σ	$^{178}Hf/^{177}Hf$	$^{180}Hf/^{177}Hf$	$Sig_{Hf\ (V)}$ [b]	$^{176}Hf/^{177}Hf$	±2σ [c]
Quartz monzonite									
ACIC0018	0.0143	12	0.00040	3	1.46718	1.88679	12	0.282159	16
ACIC0019	0.0177	15	0.00050	3	1.46721	1.88675	12	0.282152	16
ACIC0020	0.0184	15	0.00052	3	1.46721	1.88687	12	0.282161	23
ACIC0021	0.0185	15	0.00054	3	1.46720	1.88675	12	0.282169	19
ACIC0022	0.0192	16	0.00056	4	1.46724	1.88686	11	0.282149	19
ACIC0023	0.0225	18	0.00066	4	1.46719	1.88672	12	0.282140	21
ACIC0024	0.0201	21	0.00059	5	1.46720	1.88681	12	0.282149	18
ACIC0025	0.0180	15	0.00053	3	1.46725	1.88684	10	0.282159	22
ACIC0026	0.0151	13	0.00045	3	1.46723	1.88678	10	0.282180	23
ACIC0027	0.0204	17	0.00062	4	1.46724	1.88684	11	0.282157	24
ACIC0028	0.0220	20	0.00061	4	1.46718	1.88671	11	0.282165	17
ACIC0029	0.0174	22	0.00053	5	1.46726	1.88678	11	0.282182	27
ACIC0030	0.0237	20	0.00071	5	1.46722	1.88679	11	0.282152	17
ACIC0031	0.0169	20	0.00054	6	1.46722	1.88679	11	0.282151	25
ACIC0032	0.0236	21	0.00067	5	1.46716	1.88685	11	0.282128	19
ACIC0033	0.0251	21	0.00073	5	1.46718	1.88689	12	0.282134	19
ACIC0034	0.0231	22	0.00069	6	1.46722	1.88682	11	0.282134	16
ACIC0035	0.0211	20	0.00063	5	1.46723	1.88693	11	0.282150	17
ACIC0036	0.0243	19	0.00071	4	1.46722	1.88692	11	0.282139	20
ACIC0037	0.0144	15	0.00043	4	1.46721	1.88682	12	0.282163	19
ACIC0038	0.0165	18	0.00049	4	1.46725	1.88686	13	0.282168	19
ACIC0039	0.0209	50	0.00061	14	1.46721	1.88675	11	0.282169	16
ACIC0040	0.0118	12	0.00036	3	1.46723	1.88680	11	0.282133	18
ACIC0041	0.0187	17	0.00054	4	1.46714	1.88685	12	0.282125	29
ACIC0042	0.0203	23	0.00058	6	1.46722	1.88681	11	0.282168	20
ACIC0043	0.0182	15	0.00053	3	1.46724	1.88681	12	0.282175	18
Monzogabbro									
ACIC0053	0.0171	14	0.00047	3	1.46724	1.88674	10	0.282206	20
ACIC0054	0.0275	22	0.00073	4	1.46724	1.88681	9	0.282207	18
ACIC0055	0.0228	18	0.00062	4	1.46719	1.88669	10	0.282195	18
ACIC0056	0.0174	14	0.00049	3	1.46719	1.88681	9	0.282201	20
ACIC0057	0.0389	32	0.00103	6	1.46718	1.88682	9	0.282208	24
ACIC0058	0.0301	25	0.00082	5	1.46720	1.88685	10	0.282196	25
ACIC0059	0.0601	50	0.00155	9	1.46724	1.88676	11	0.282147	20
ACIC0060	0.0321	27	0.00088	5	1.46722	1.88677	9	0.282200	24
ACIC0061	0.0384	37	0.00106	9	1.46725	1.88684	11	0.282164	19
ACIC0062	0.0265	23	0.00078	5	1.46721	1.88683	10	0.282170	18
ACIC0063	0.0564	49	0.00154	10	1.46717	1.88667	8	0.282188	19
ACIC0064	0.0383	36	0.00103	8	1.46722	1.88678	10	0.282177	16
ACIC0065	0.0348	28	0.00099	6	1.46720	1.88685	9	0.282185	21
ACIC0066	0.0154	15	0.00045	4	1.46718	1.88680	13	0.282157	20
ACIC0067	0.0208	19	0.00060	4	1.46730	1.88694	10	0.282208	18
ACIC0068	0.0088	8	0.00027	2	1.46723	1.88689	14	0.282204	21
ACIC0069	0.0136	12	0.00041	3	1.46721	1.88685	10	0.282203	18
ACIC0070	0.0297	25	0.00085	6	1.46721	1.88688	13	0.282180	23
ACIC0071	0.0362	42	0.00098	10	1.46718	1.88663	11	0.282162	39
ACIC0072	0.0368	33	0.00101	7	1.46722	1.88678	9	0.282175	52
ACIC0073	0.0108	9	0.00030	2	1.46723	1.88678	12	0.282197	18
ACIC0074	0.0170	17	0.00049	4	1.46720	1.88685	11	0.282208	26
ACIC0075	0.0523	63	0.00142	14	1.46724	1.88685	11	0.282149	18
ACIC0076	0.0328	29	0.00088	6	1.46723	1.88686	10	0.282172	19
ACIC0077	0.0171	17	0.00047	3	1.46725	1.88683	12	0.282204	27
ACIC0078	0.0242	20	0.00068	4	1.46722	1.88683	11	0.282189	20
ACIC0079	0.0173	14	0.00046	3	1.46720	1.88680	12	0.282200	24

Spot	$^{176}Hf/^{177}Hf_{(t)}$ [d]	εHf(t) [d]	±2σ [c]	Avg MORB (Ga) [e]	T_{DM2} (Ga) [f]	Age (Ma) [g]	±2σ
Quartz monzonite							
ACIC0018	0.282155	-11.57	0.87589	1.77	1.75	479.64	1
ACIC0019	0.282147	-11.87	0.88028	1.79	1.76	479.01	1
ACIC0020	0.282156	-11.38	0.88085	1.77	1.74	487.20	1
ACIC0021	0.282164	-11.19	0.88097	1.76	1.73	483.11	1
ACIC0022	0.282143	-12.04	0.88303	1.80	1.77	477.87	1
ACIC0023	0.282134	-12.06	0.88736	1.81	1.78	492.02	1
ACIC0024	0.282143	-11.95	0.89330	1.80	1.77	481.46	1
ACIC0025	0.282153	-11.63	0.88116	1.78	1.75	479.58	1
ACIC0026	0.282175	-10.66	0.87747	1.73	1.70	488.16	1
ACIC0027	0.282151	-11.64	0.88480	1.78	1.75	483.33	1
ACIC0028	0.282159	-11.24	0.89005	1.76	1.74	488.90	1
ACIC0029	0.282176	-10.70	0.89638	1.73	1.70	485.38	1
ACIC0030	0.282145	-11.79	0.88996	1.79	1.76	486.80	1
ACIC0031	0.282145	-11.39	0.89036	1.78	1.76	503.99	1
ACIC0032	0.282121	-12.93	0.89333	1.84	1.81	472.35	1
ACIC0033	0.282127	-12.35	0.89310	1.82	1.80	489.24	1
ACIC0034	0.282127	-12.60	0.89630	1.83	1.80	477.82	1
ACIC0035	0.282144	-11.94	0.89183	1.80	1.77	481.57	1
ACIC0036	0.282133	-13.31	0.88969	1.83	1.81	436.61	1
ACIC0037	0.282159	-11.39	0.88080	1.77	1.74	481.74	1
ACIC0038	0.282163	-11.28	0.88595	1.76	1.73	480.49	1
ACIC0039	0.282163	-11.26	1.00140	1.76	1.73	481.74	1
ACIC0040	0.282130	-12.30	0.87664	1.82	1.79	487.77	1
ACIC0041	0.282120	-12.73	0.88430	1.84	1.81	484.58	1
ACIC0042	0.282163	-11.30	0.89836	1.76	1.73	480.04	1
ACIC0043	0.282170	-11.07	0.88063	1.75	1.72	479.13	1
Monzogabbro							
ACIC0053	0.282202	-9.71	0.87919	1.68	1.65	489.41	1
ACIC0054	0.282200	-9.80	0.89625	1.68	1.66	488.054	1
ACIC0055	0.282189	-10.22	0.88756	1.71	1.68	487.25	1
ACIC0056	0.282196	-10.26	0.87998	1.70	1.67	474.12	1
ACIC0057	0.282222	-36.34	0.92385	2.09	2.10	-750.01	1
ACIC0058	0.282188	-10.20	0.90348	1.71	1.68	489.75	1
ACIC0059	0.282131	-11.89	0.99926	1.81	1.78	503.31	1
ACIC0060	0.282192	-10.15	0.90878	1.70	1.67	484.98	1
ACIC0061	0.282154	-11.28	0.94430	1.77	1.74	495.09	1
ACIC0062	0.282162	-10.50	0.89818	1.75	1.72	516.50	1
ACIC0063	0.282173	-10.59	0.99651	1.73	1.70	494.92	1
ACIC0064	0.282167	-10.89	0.94117	1.75	1.72	491.23	1
ACIC0065	0.282175	-10.42	0.91306	1.73	1.70	499.63	1
ACIC0066	0.282152	-11.25	0.88052	1.77	1.74	499.34	1
ACIC0067	0.282202	-9.51	0.88921	1.68	1.65	497.53	1
ACIC0068	0.282201	-9.70	0.87173	1.68	1.65	490.72	1
ACIC0069	0.282199	-9.69	0.87629	1.68	1.66	494.35	1
ACIC0070	0.282172	-10.32	0.90483	1.73	1.70	509.32	1
ACIC0071	0.282153	-11.49	0.96608	1.78	1.75	487.08	1
ACIC0072	0.282165	-10.56	0.92960	1.74	1.71	509.60	1
ACIC0073	0.282194	-9.87	0.87324	1.69	1.67	494.69	1
ACIC0074	0.282203	-9.59	0.88461	1.68	1.65	492.19	1
ACIC0075	0.282135	-11.61	1.07282	1.80	1.77	509.26	1
ACIC0076	0.282164	-10.91	0.91658	1.75	1.72	495.88	1
ACIC0077	0.282199	-8.84	0.88455	1.67	1.64	533.16	1
ACIC0078	0.282183	-10.33	0.89054	1.72	1.69	491.68	1
ACIC0079	0.282195	-9.826	0.87967	1.69	1.66	494.98	1

Standards	$^{176}Yb/^{177}Hf$ [a]	±2σ	$^{176}Lu/^{177}Hf$ [a]	±2σ	$^{178}Hf/^{177}Hf$	$^{180}Hf/^{177}Hf$	Sig_{Hf} (V)[b]	$^{176}Hf/^{177}Hf$	±2σ [c]	$^{176}Hf/^{177}Hf_{(t)}$[d]	εHf(t) [d]	±2σ [c]	Age (Ma)
Blue Berry (BB)													
Spot0001	0.0055	5	0.00015	1	1.46718	1.886	10	0.28166	20	0.281663	-27.21	0.86	560
Spot0002	0.0056	6	0.00015	1	1.46722	1.886	10	0.28168	21	0.281681	-26.58	0.86	560
Spot0004	0.0057	7	0.00015	1	1.46724	1.886	10	0.28166	23	0.281662	-27.26	0.86	560
Spot0005	0.0059	5	0.00016	1	1.46720	1.886	10	0.28165	16	0.281656	-27.44	0.86	560
Spot0044	0.0058	7	0.00016	2	1.46719	1.886	10	0.28165	19	0.281657	-27.42	0.86	560
Spot0045	0.0059	5	0.00016	1	1.46722	1.886	10	0.28166	20	0.281665	-27.13	0.86	560
Spot0080	0.0057	5	0.00015	1	1.46722	1.886	10	0.28166	19	0.281661	-27.28	0.86	560
Spot0081	0.0057	5	0.00015	1	1.46723	1.886	10	0.28167	19	0.281669	-27.00	0.86	560
Spot0082	0.0056	5	0.00015	1	1.46731	1.886	10	0.28169	19	0.281694	-26.12	0.86	560
Mean	0.0057		0.00015		1.4672	1.886		0.2817		0.2817	-27.21		560
GJ-1													
Spot0011	0.0087	10	0.00025	3	1.46720	1.886	8	0.28202	26	0.282022	-13.55	0.87	602
Spot0012	0.0087	7	0.00025	2	1.46722	1.886	8	0.28200	16	0.281997	-14.42	0.87	602
Spot0013	0.0087	7	0.00025	2	1.46717	1.886	7	0.28200	22	0.281997	-14.42	0.87	602
Spot0014	0.0086	10	0.00025	2	1.46718	1.886	7	0.28198	20	0.281981	-15.02	0.87	602
Spot0015	0.0086	11	0.00025	3	1.46724	1.886	7	0.28201	19	0.282008	-14.06	0.87	602
Spot0050	0.0085	23	0.00025	6	1.46722	1.886	8	0.28199	24	0.281989	-14.74	0.89	602
Spot0051	0.0085	7	0.00025	1	1.46721	1.886	7	0.28201	22	0.282008	-14.05	0.87	602
Spot0052	0.0086	7	0.00025	1	1.46718	1.886	8	0.28197	18	0.281967	-15.50	0.87	602
Spot0086	0.0087	7	0.00025	1	1.46721	1.886	8	0.28200	20	0.282001	-14.28	0.87	602
Spot0088	0.0086	7	0.00024	1	1.46721	1.886	8	0.28199	16	0.281989	-14.73	0.87	602
Mean	0.0086		0.0002		1.4672	1.886		0.2820		0.2820	-14.42		602
Mudtank													
Spot0006	0.0013	1	0.00003	0	1.46719	1.886	11	0.28251	21	0.282511	6.70	0.86	732
Spot0007	0.0013	1	0.00003	0	1.46719	1.886	11	0.28250	20	0.282501	6.32	0.86	732
Spot0008	0.0014	2	0.00003	0	1.46721	1.886	11	0.28249	29	0.282496	6.16	0.87	732
Spot0009	0.0013	1	0.00003	0	1.46725	1.886	11	0.28252	18	0.282522	7.09	0.86	732
Spot0010	0.0013	2	0.00003	0	1.46722	1.886	11	0.28248	21	0.282487	5.83	0.86	732
Spot0047	0.0012	1	2.8E-05	0	1.46725	1.886	11	0.28251	17	0.282514	6.78	0.86	732
Spot0048	0.0012	1	2.9E-05	0	1.46721	1.886	11	0.28250	20	0.282505	6.48	0.86	732
Spot0049	0.0012	1	2.9E-05	0	1.46720	1.886	11	0.28250	23	0.282503	6.39	0.86	732
Spot0083	0.0012	1	3.0E-05	0	1.46724	1.886	11	0.28250	18	0.282499	6.26	0.86	732
Spot0084	0.0012	1	2.9E-05	0	1.46721	1.886	11	0.28251	18	0.282511	6.69	0.86	732
Spot0085	0.0014	1	3.4E-05	0	1.46728	1.886	10	0.28254	21	0.282542	7.78	0.87	732
Mean	0.0013		0.0000		1.4672	1.886		0.2825		0.2825	6.48		732

a= $^{176}Yb/^{177}Hf = (^{176}Yb/^{173}Yb)_{true}$ x $(^{173}Yb/^{177}Hf)_{measured}$ x $(m^{173}(Yb)/m^{177}(Hf))b(Hf)$, $b(Hf) = \ln(^{179}Hf/^{177}Hf_{true} / {}^{179}Hf/^{177}Hf_{measured}) / \ln(m^{179}(Hf)/m^{177}(Hf))$. m=mass of respective isotope. The $^{176}Lu/^{177}Hf$ were calculated in a similar way by using the $^{175}Lu/^{177}Hf$ and b(Yb);

b= Mean Hf signal in volt;

c= Uncertainties are quadratic additions of the within-run precision and the reproducibility of the standard zircons;

d= Initial $^{176}Hf/^{177}Hf$ and ƐHf calculated using the estimated Pb-Pb ages of respective zircon domains, and the CHUR parameters: $^{176}Lu/^{177}Hf = 0.0336$, and $^{176}Hf/^{177}Hf = 0.282785$ (Bouvier et al., 2008);

e= Avg MORB calculated based on Chauvel et al. (2008);

f= Avg T_{DM} calculated based on Dhuime et al. (2011);

g= U-Pb ages determined by LA-ICP-MS;